Australian Government

Department of Defence
Defence Science and
Technology Group

Radar Detection Performance in Medium Grazing Angle X-band Sea-clutter

Luke Rosenberg [1] *and Stephen Bocquet* [2]

[1] **National Security and ISR Division**

[2] **Joint and Operations Analysis Division**

Defence Science and Technology Group

DST-Group–TR–3193

ABSTRACT

This report describes the target detection performance of an airborne surface surveillance radar in the presence of medium grazing angle sea-clutter. In the absence of frequency agility, the temporal correlation of the sea-clutter can be significant and if it is not accounted for in the radar model, the required signal to interference ratio for a given probability of detection, P_d, will be incorrect by several dB, resulting in over-estimated performance. This report describes a robust method for calculating the P_d for both K and Pareto compound sea-clutter distributions. Empirical models of the amplitude distribution and the speckle correlation are used to determine the expected detection performance given different collection geometries and environmental conditions with the output used to determine the minimum detectable target radar cross section in a detection scenario.

RELEASE LIMITATION

Approved for Public Release

APPROVED FOR PUBLIC RELEASE

Radar Detection Performance in Medium Grazing Angle X-band Sea-clutter

Executive Summary

This report summarises the target detection performance of an X-band surface surveillance radar operating at medium grazing angles in the maritime environment. A number of different detection scenarios are explored with variations in the collection geometry, sea-state and polarisation. Two sea-clutter distributions are considered: the popular K-distribution and the Pareto distribution which has recently been shown to be a better match to the distribution tail. Consequently, detection performance results using the Pareto distribution have been chosen as 'truth' in the report.

To test these scenarios, a number of parameter models are required to relate the radar and environmental characteristics to the mean backscatter and distribution shape values. Appropriate models are therefore presented along with a full mathematical description of the different target fluctuation models. A major contribution of the report is a full derivation of the Ward, Tough and Watts detection algorithm for correlated clutter with a modification to make the technique robust for high clutter to noise ratios.

The sea-clutter and target detection models are then used to analyse the probability of false alarm, P_{fa}, probability of detection, P_{d} and the minimum detectable radar cross section (RCS) for a given set of radar parameters. The P_{fa} results show a big difference in the horizontal polarisations (HH and HV) with the K distribution underestimating the threshold by up to 5 dB, while there is only a minor difference in the vertical channel (VV). The effect of non-coherently integrating pulses is to reduce the threshold.

A comparison of the target fluctuation models reveals that the P_{d} curve is steeper for the chi-squared distribution model than the exponential model. Increasing the target correlation reduces the slope for both models, with the effect being more pronounced for the exponential model. Using a distribution model also allows us to extrapolate down to lower P_{fa} levels than could be used in a real detection scheme. By comparing P_{fa} levels, it is found that for the HH polarisation, there is a larger difference in the signal to interference ratio between the K and Pareto distributions. This mismatch also got larger as the P_{fa} reduced.

Further analysis of the detection performance with varying azimuth, grazing and sea-state reveals that the choice of model is critical to accurately determine the detection performance. There is significant mismatch between the K and Pareto distribution results, particularly for the HH polarisation. Other large discrepancies are observed in the cross wind direction and at lower grazing angles. The mismatch for the VV polarisation is typically very small.

The final result looked at the minimum detectable target RCS given a set of radar parameters. For the lower grazing angles in the HH and HV channels, there was a large difference between the K and Pareto distributions, which reduced as the grazing angle increased. The two distributions gave almost identical results for the VV channel. In terms of detectability, the Pareto result shows that the HV polarisation has the smallest target RCS, then VV and HH.

Authors

Luke Rosenberg
National Security and ISR Division

Luke Rosenberg received his BE (Elec.) with honours from Adelaide University in 1999 and joined the DST Group in January 2000. Since this time he has completed both a masters degree in signal and information processing and a PhD in multichannel synthetic aperture radar through Adelaide University. He has worked at the DST Group as an RF engineer in the missile simulation centre and now as a research scientist working in the areas of radar and clutter modelling, radar imaging and detection theory.

Stephen Bocquet
Joint and Operations Analysis Division

Stephen Bocquet completed his BSc in Physics and Mathematics at the University of Canterbury, Christchurch, New Zealand in 1983, and his MSc (Hons) in Physics in 1987. He received his PhD in Physics from Monash University in 1993, and joined the DST Group of Australia the same year. He currently works in operations analysis with the Joint and Operations Analysis Division of DST Group, while maintaining an active research interest in radar sea clutter.

THIS PAGE IS INTENTIONALLY BLANK

Contents

Figures

Tables

THIS PAGE IS INTENTIONALLY BLANK

Glossary

CCDF: Complimentary Cumulative Distribution Function

CFAR: Constant False Alarm Rate

CNR: Clutter to Noise Ratio

DST Group: Defence Science and Technology Group

HH: Horizontal transmit and Horizontal receive polarisation

HV: Horizontal transmit and Vertical receive polarisation

IRSG: Imagery Radar Systems Group

MAST06: Maritime Surveillance Trial 2006

PDF: Probability Density Function

PRF: Pulse Repetition Frequency

RCS: Radar Cross Section

RF: Radio Frequency

SAR: Synthetic Aperture Radar

SCT04: Sea Clutter Trial 2004

SIR: Signal to Interference Ratio

TSC: Technology Services Corporation

VV: Vertical transmit and Vertical receive polarisation

WTW: Ward, Tough and Watts

THIS PAGE IS INTENTIONALLY BLANK

1   Introduction

This report is concerned with quantifying the detection performance of an X-band surface surveillance radar in the maritime environment. The results are based on data from DST Group's Ingara radar which has collected 12 days of fine resolution fully polarimetric sea-clutter data in a circular spotlight mode covering all azimuth angles and focussing on the medium grazing angle region, $15° − 45°$. This data has been used to characterise the statistical properties of the sea-clutter in order to accurately quantify target detection performance. These include the mean radar backscatter [Crisp et al. 2008], amplitude distribution [Dong 2006, Rosenberg, Crisp & Stacy 2010b, Weinberg 2011a, Rosenberg & Bocquet 2015, Rosenberg, Watts & Bocquet 2014] Doppler spectrum [Rosenberg 2014] and sea spikes [Rosenberg 2013].

These studies then led to a number of empirical models which take into account different combinations of the polarisation, collection geometry and environmental conditions. Relevant models include the imaging radar systems group (IRSG) mean backscatter model [Crisp et al. 2008], the short-time temporal correlation [Rosenberg 2014] and the K distribution shape parameter [Rosenberg, Crisp & Stacy 2009, Crisp, Rosenberg & Stacy 2015]. To effectively model the effect of sea-spikes, the latter model has also been modified and applied to the Pareto distribution shape [Rosenberg et al. 2015]. These empirical models are described in Section 2 of the report.

Parametric modelling is a useful tool to predict a radar's target detection performance given a statistical description of the environment. Once a clutter model has been chosen and its parameters determined, a threshold can be determined based on the desired probability of false alarm, P_{fa}, to ensure a CFAR (Constant False Alarm Rate). Any backscatter response above the threshold is then declared to be a potential target. Using this threshold, a probability of detection P_d can be calculated for a given target fluctuation model to determine the required signal to interference (clutter and noise) ratio (SIR). Subsets of the empirical parameter models have previously been used to analyse target detection performance in K and KK distributed sea clutter [Rosenberg & Crisp 2010a] and to study the impact of temporal correlation with different fluctuating targets [Rosenberg 2012, Rosenberg & Bocquet 2013b]. These studies found that if the correct distribution was not used to model the tail of the distribution and if the temporal correlation was not accounted for, then the required SIR for a desired P_d can be over-estimated by up to several dB.

The main contribution of this report to provide a comprehensive mathematical description of the modelling framework and to extend the previous results using the newly developed Pareto shape model. Section 3 describes the modelling framework for different fluctuating targets using different sea-clutter distributions. A full derivation of the Ward, Tough & Watts [2013] detection algorithm for correlated clutter and /or targets is then presented with the modification [Rosenberg & Bocquet 2013b] which makes the technique robust for high clutter to noise ratios (CNR).

The final Section 4 then uses the empirical models to quantify the detection performance for a number of different geometries and environmental conditions. Due to its good fit to the Ingara sea clutter data [Rosenberg & Bocquet 2013a], the Pareto distribution is used as a proxy for the data with the K-distribution results showing the mismatch that would be expected in a detection scenario. These results are then fed into the radar range equation to determine the minimum detectable radar cross section (RCS) for a given set of radar parameters.

2 Sea-clutter models

To comprehensively characterise target detection performance, [Ward, Tough & Watts 2013] state that knowledge of the following sea-clutter, radar processing and environmental characteristics is required:

- mean backscatter
- amplitude statistics
- temporal correlation or spectrum
- spatial characteristics and correlations
- discrete clutter spike characteristics
- carrier frequency
- polarisations
- spatial resolution
- use of frequency agility
- grazing angle
- wind-speed and direction
- sea-swell and direction

To this end, a number of experiments were conducted using the Ingara X-band radar to collect sea-clutter covering as many different combinations of these parameters as possible. A description of the trials and the collected data is presented in Section 2.1.

Detection performance requires an accurate representation of the amplitude or intensity probability distribution function (PDF). The most commonly used PDF model for sea-clutter is the K-distribution as it captures the bulk of the sea-clutter PDF very well. It was first applied to modelling probability distributions of sea-clutter by Jakeman & Pusey [1976] and was later put into a Bayesian or compound formulation by Ward [1981]. This allows a more meaningful understanding of the two main components - these being the temporal or fast varying component and the slowly varying texture component. The fast component is commonly known as speckle and is the result of constructive and destructive interference effects between multiple scatterers. It is typically associated with the small local wind-driven ripples (capillary waves) on the ocean surface. The texture component represents changes in the large and medium scale waves which modulate the speckle. In terms of scattering processes, reflections off the wind-driven ripples are known as Bragg (or resonant) scattering, while the non-Bragg scattering can be described as a combination of whitecaps and discrete sea-spikes [Ward, Tough & Watts 2013]. It is these sea-spikes which cause the K-distribution model to break down, particularly at finer resolutions where the average backscatter reduces and the sea-spikes cause higher levels of backscatter relative to the mean, hence extending the tail of the distribution.

In order to better model this effect, the KA [Middleton 1999], KK [Dong 2006, Rosenberg, Crisp & Stacy 2010*b*], Pareto [Balleri, Nehorai & Wang 2007, Farshchian & Posner 2010, Weinberg 2011*b*, Rosenberg & Bocquet 2015] and K+Rayleigh [Lamont-Smith 2000, Rosenberg, Watts & Bocquet 2014] models have been proposed. The KA model was originally proposed by Middleton [1999] and then specifically applied to spiky sea clutter by [Ward & Tough 2002, Ward, Tough & Watts 2013]. A comparison of this model and the KK distribution has been applied to the Ingara data [Dong 2006]. The KK distribution offered a better fit, but relied on fitting up to five parameters. A number of optimal and sub-optimal detectors have also been proposed, but they are difficult

to implement in practice [Weinberg 2012*a*]. This led to the Pareto model which is described by two parameters, yet can reasonably model the long tails present in the sea-clutter distribution. The Pareto distribution also has significantly simpler optimal and sub-optimal detectors [Weinberg 2012*b*, Weinberg 2014].

Clearly the PDF must account for the different elements of the sea-clutter as well as the thermal noise in the radar. Therefore, the first element required for modelling is the CNR which is described in Section 2.2. This is determined using the thermal noise power and clutter power (radar range) equations [Ward, Tough & Watts 2013] with the IRSG mean backscatter model [Crisp et al. 2008] used to provide variation with the viewing geometry, sea state and polarisation. The K and Pareto distributions are then described in Section 2.3, with details on how each of the shape parameters were estimated. The newly developed shape model for these distributions [Rosenberg et al. 2015] is also presented in this section.

To improve the probability of detection, a radar will typically average returns from multiple looks - pulses and/or scans. This reduces the variance of the random interference and increases the mean separation with the target signal component. In the absence of frequency agility, there may be little difference in the radar return when looking at the same clutter patch closely in time. This effect is known as temporal correlation and is often characterised from its Fourier transform or in this context, its radar Doppler spectrum. There is a large body of literature focussed on understanding the radar Doppler spectrum [Long 2001, Ward, Tough & Watts 2013, Plant 1997]. From this analysis came two significant models describing the line shape of the mean Doppler spectrum from low grazing angles [Lee et al. 1995, Walker 2001]. The former uses a Gaussian component to model the Bragg scatterers and a Lorentzian and/or Voigtian for the non-Bragg components. A simpler model was later presented by Walker [2001], who uses a combination of three Gaussians to describe the Bragg, whitecap and sea-spike components of the Doppler spectrum. At medium grazing angles, a modified two component model was presented by Rosenberg [2014] to model the Ingara data. This led to a simple model for temporal decorrelation as a function of the wind speed and wave height. This final empirical model is presented in Section 2.4 with details on how to account for platform motion and antenna scanning.

2.1 Trials background

The trial data was obtained with Ingara on two separate occasions and at two distinctly different regions. The first 'sea-clutter' trial was conducted in 2004 (SCT04) in the Southern Ocean approximately 100 km south of Port Lincoln, South Australia [Crisp, Stacy & Goh 2006]. The site chosen was at the edge of the Australian continental shelf where there was little chance of shallow water affecting the wave field. During the trial, ocean backscatter was collected for a range of different geometries on eight separate days with different ocean conditions. The second 'maritime surveillance' trial was conducted in 2006 (MAST06) in littoral and open sea environments near Darwin in the Northern Territory. Again, data was collected for a range of different geometries and ocean conditions. In this trial, a total of four days data were collected: two of the days were in the littoral zone approximately 25 km north of Darwin and the other two days were in the open ocean approximately 200 km west of Darwin.

During the ocean backscatter collections, Ingara was operated in the circular spotlight-mode. Figure 1 shows the collection geometry for this mode, where the aircraft flies a circular orbit in an anti-clockwise direction (as seen from above) around a nominated point of interest, while the radar beam is continuously directed toward this point. Radar echo data is continuously collected

during the full $360°$ orbit, with the instantaneous pulse repetition frequency (PRF) appropriately adjusted to maintain a constant spatial pulse separation between pulse transmission positions. Once collected, the echo data may be processed either immediately (in real-time) or subsequently (off-line) to produce either range-compressed profiles or spotlight synthetic aperture radar (SAR) images of the scene at various azimuth angles. Further, owing to the continuous nature of the data collection, the images can be formed at any desired azimuth look direction. Each collection of data in this mode is referred to as a 'run' and there may be several complete orbits in a single run.
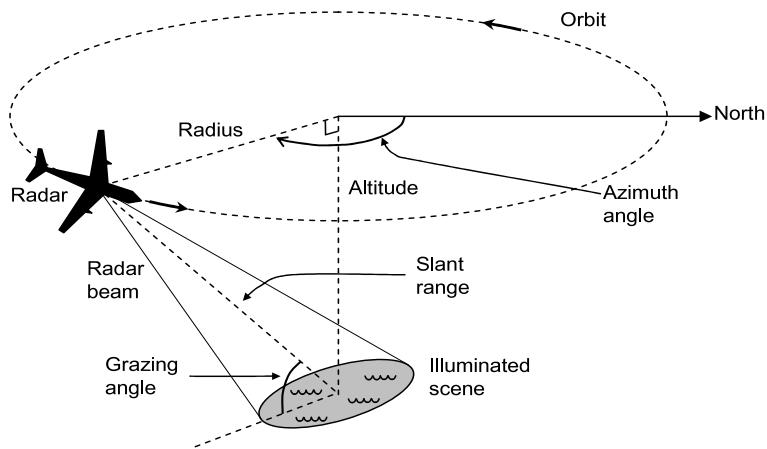
Figure 1: Circular spotlight mode collection geometry used for both Ingara sea clutter trials.

In order to examine the effect of grazing angle on ocean backscatter, runs were made with different altitude and orbit diameters. For both the SCT04 and MAST06 trials, data was collected at the centre of the spotlight for the nominal grazing angles of $15°$ to $45°$ in $5°$ increments. Owing to the finite beam width of the radar, its footprint on the ocean surface has a significant range extent. This means that the grazing angle varies across the footprint. It follows that, with appropriate range compression and data processing, the variation in backscatter with grazing angle across the range extent of the radar beam footprint can be measured. In this way, backscatter measurements for most grazing angles in the range from $15°$ to $45°$ could be extracted from the data.

The aircraft speed was approximately 200 knots and so a 1.5 nautical mile (NM) radius orbit took approximately 3 minutes while a 1.9 NM radius orbit took about 4 minutes. The total collection across all grazing angles took approximately 90 minutes. It is reasonable to assume that over such short time intervals, the ocean surface conditions are relatively unchanged and that mean backscatter variations are mostly due to the changing imaging geometry rather than changing ocean conditions. Nevertheless, it is possible that wind gusts and changes of wind strength and direction may have affected the measurements. Table 1 shows the wind and wave ground truth for the data used in this report.

Finally, using the geometry in Figure 1, the azimuth resolution can be calculated approximately by $R\phi_{3dB}$, where R is the slant range and ϕ_{3dB} is the measured two-way azimuth antenna 3 dB beam width equal to $1.02°$ for the horizontal transmit, horizontal receive (HH) channel and $0.99°$ for the vertical transmit, vertical receive (VV). Table 2 shows the geometry for collections at a range of grazing angles and slant-ranges for a beam width of $1°$. Over these nominal parameters, the average azimuth resolution is 62.7 m. However since each collection spans a range of grazing angles, the actual azimuth resolution will always differ slightly.

Table 1: Wind and wave ground truth. Directions are "from" not "to".

Trial	Flight	Date	Wind		Wave		
			Speed (m/s)	Direction (°)	Height (m)	Direction (°)	Period (s)
SCT04	F33	9/8/04	10.2	248	4.9	220	12.3
SCT04	F34	10/8/04	7.9	248	3.5	205	11.8
SCT04	F35	11/8/04	10.3	315	2.6	210	10.4
SCT04	F36	12/8/04	13.6	0	3.2	293	8.8
SCT04	F37	16/8/04	9.3	68	2.5	169	9.7
SCT04	F39	20/8/04	9.5	315	3.0	234	11.4
SCT04	F40	24/8/04	13.2	22	3.8	254	12.2
SCT04	F42	27/8/04	8.5	0	4.3	243	12.5
MAST06	F2	17/5/06	8.5	115	0.62	112	3.1
MAST06	F4	19/5/06	3.6	66	0.25	35	2.6
MAST06	F8	23/5/06	3.5	83	0.41	46	4.0
MAST06	F9	24/5/06	10.2	124	1.21	128	4.6

Table 2: Nominal geometric parameters of circular spotlight-mode collections.

Grazing angle (°)	Altitude (m)	Radius (NM / m)	Slant range (m)	Azimuth res. (m)
15	932	1.9 / 3519	3643	63.54
20	1353	1.8 / 3334	3548	62.80
25	1522	1.8 / 3334	3679	63.97
30	1711	1.6 / 2963	3421	59.72
35	2073	1.6 / 2963	3617	63.11
40	2314	1.5 / 2778	3626	63.10

2.2 Clutter and noise mean power

Simulating radar performance requires accurate models for the mean power of the clutter, noise and target. To measure the performance, the target power is typically varied with respect to the interference or clutter plus noise power. The mean clutter power, p_c is determined by the radar range equation:

$$p_c = \frac{P_t G^2 \lambda_c^2 \sigma_c T_p B}{(4\pi)^3 R^4 L_a L_s} \tag{1}$$

where P_t is the transmit power, G is the one-way gain on transmit and receive, λ_c is the radar wavelength, R is the slant range, σ_c is the sea-clutter RCS, L_a and L_s represent the atmospheric and system losses respectively and pulse compression adds a gain given by the pulse length - bandwidth product, $T_p B$. The thermal noise power in the radar can be defined as,

$$p_n = k_{\text{boltz}} T_0 B F_n \tag{2}$$

where k_{boltz} is Boltzmann's constant, T_0 is the reference temperature and F_n is the radar noise figure. The next section gives further detail of the parameters in Equation 1. Section 2.2.2 then presents the Imaging Radar Systems Group (IRSG) mean backscatter model which captures the mean backscatter as a function of azimuth, grazing and wind speed. These are then all brought together with a model for the CNR in Section 2.2.3.

2.2.1 Parameter description

There are many parameters in Equation 1 which are required to accurate represent the CNR. The values chosen for this analysis are now described in more detail:

Transmit power, P_t The peak power of a typical airborne radar is 20 kW.

Radar wavelength, λ_c For an X-band radar with a centre frequency, f_c of 10 GHz, the wavelength is 3 cm.

Antenna gain, G The one-way antenna gain is related to the wavelength and the effective area of the antenna aperture. For the modelling in this report, an antenna gain of 35 dB has been used.

Slant range, R The slant range is related to the altitude of the radar, h, the grazing angle, θ and the mean radius of the earth, $R_\mathrm{e} = 6.4 \times 10^3$ km. The earth radius is typically multiplied by 4/3 to account for the average effect of atmospheric refraction, giving an effective radius $E = 4/3 R_\mathrm{e}$. The slant range to the sea surface is obtained by solving equation (12.10) of [Ward, Tough & Watts 2013] for R:

$$R = \sqrt{E^2 \sin^2 \theta + 2Eh + h^2} - E \sin \theta$$
$$\approx \frac{h(1 + h/E)}{\sin \theta + h/E}. \tag{3}$$

The flat earth approximation is $R \approx h/\sin\theta$, which is quite accurate unless the grazing angle is small. For example, if the radar altitude is 10 km (33.1 thousand feet) and the grazing angle is $30°$, the flat earth approximation for the slant range is 20 km, whereas the more accurate calculation gives a result just 35 m less than this.

Sea-clutter RCS, σ_c The radar cross section[1] can be described in terms of the mean backscatter σ_0 within a given resolution cell with area A_cell,

$$\sigma_c = \sigma_0 A_\mathrm{cell}. \tag{4}$$

The mean backscatter is modelled using the IRSG model described below, while the ground plane area, A_cell is given by the slant range and azimuth resolutions, Δ_x, Δ_y projected onto the ground,

$$A_\mathrm{cell} = \Delta_x \Delta_y \sec \theta \tag{5}$$

with range and azimuth resolutions given by,

$$\Delta_x = \frac{v_c}{2B},$$
$$\Delta_y \approx R \phi_{3dB} \tag{6}$$

where v_c is the speed of light. For a bandwidth of 200 MHz, the range resolution is 0.75 m. For the azimuth resolution, with a beam width of $1°$, the resolution varies according to the grazing angle. For the Ingara flight trials, the azimuth resolution was approximately 63 m (see Table 2).

---

[1]Note that the propagation factor is inherently included in this definition. Atmospheric losses have been included in the loss term, L_a.

Atmospheric loss, L_a The atmospheric loss, L_a describes all the losses in the atmosphere. A loss of 2 dB has been chosen for this analysis.

System loss, L_s The system loss, L_s is a bulk term which describes all the losses in the radar system. A loss of 5 dB has been chosen for this analysis.

Pulse compression gain, $T_p B$ Pulse compression adds a gain to the radar range equation based on the pulse length, T_p and the system bandwidth. For a pulse width of $5 \mu s$ and a bandwidth of 200 MHz, the gain is 1000.

Temperature, T_0 The ambient temperature is set to 290 K.

Noise figure, F_n The system noise figure is a measure of the degradation of the signal to noise ratio caused by components in the RF signal chain. A typical value is 4 dB.

In addition to these parameters, the models for the mean backscatter and Pareto shape require the wind speed and significant wave height as inputs. For modelling purposes, it is desirable to specify a single parameter to represent these sea conditions. The Douglas sea-state, S can be related to both wind speed and significant wave height using the following relationships [Technology Service Corporation 1990]:

$$U = 3.2 S^{0.8}, \tag{7}$$

$$H_{1/3} = 0.024 U^2. \tag{8}$$

2.2.2 IRSG mean backscatter model

There are a number of existing models for the mean backscatter, although only a few cover the medium grazing angle region. The two most suited are the Technology Services Corporation (TSC) and Masuko models, [Technology Service Corporation 1990, Spaulding, Horton & Pham 2005, Masuko et al. 1986], however they are both unable to capture all the variations with the weather conditions and azimuth and grazing angles. This led to a new empirical model presented by [Crisp et al. 2008] known as the imaging radar systems group (IRSG) model. The model is applied independently to each polarisation in the log domain and uses relationships taken from [Ulaby, Moore & Fung 1982, Shimada, Kawamura & Shimada 2003]. It includes a power law model for variations in the wind speed, a linear model for the grazing and a two element Fourier series to model azimuth. The principle behind this model is that the small scale waves which are responsible for Bragg scattering from the ocean surface are directly dependent on the surface wind speed. The stronger the wind speed, the larger the capillary waves and hence the larger the backscatter. The model is valid over $20°$-$45°$ in grazing, $360°$ in azimuth and wind speeds from 3-14 m/s.

The first component of the IRSG model captures the variation in backscatter with grazing angle θ and wind speed U and is defined for the upwind, downwind and crosswind directions. If σ_0' represents the mean backscatter in one of these azimuth directions, then the relationship is given by

$$\sigma_0'(\theta, U) = a_0 + a_1 \theta + a_2 \log_{10}(U). \tag{9}$$

where the three sets of coefficients a_0, a_1 and a_2 have been determined by model fitting over the 12 days of the Ingara data. The second stage is to combine these three backscatter results into new coefficients,

$$b_0(\theta, U) = \left[\sigma'_u(\theta, U) + \sigma'_d(\theta, U) + 2\sigma'_c(\theta, U)\right]/4,$$
$$b_1(\theta, U) = \left[(\sigma'_u(\theta, U) - \sigma'_d(\theta, U)\right]/2, \tag{10}$$
$$b_2(\theta, U) = b_0(\theta, U) - \sigma'_c(\theta, U),$$

where $\sigma'_u(\cdot)$, $\sigma'_d(\cdot)$ and $\sigma'_c(\cdot)$ are the upwind, downwind and crosswind values of $\sigma'_0(\cdot)$. The final step takes these new coefficients and includes the azimuth variation, ϕ, in a two element Fourier series,

$$\sigma_0(\phi, \theta, U) = b_0(\theta, U) + b_1(\theta, U)\cos\phi + b_2(\theta, U)\cos(2\phi) \tag{11}$$

Implementing the model requires calculating Equation 9 for each wind direction using three sets of a coefficients for each azimuth direction. The mean backscatter is then determined by substituting the angle specific backscatter values into Equation 10 and then using that result in Equation 11. The 9 coefficients required to implement the model are given in Table 3 for each polarisation. Figure 2 shows an example of the F35 data set with the wind speed taken from Table 1. Clearly the trends have been well captured in the model with a sinusoidal variation across azimuth and increasing mean backscatter as the grazing angle increases.

Table 3: Mean backscatter coefficients.

	Azimuth	a_0	a_1	a_2
	Upwind	-60.03	23.39	22.65
HH	Downwind	-67.80	28.58	23.92
	Crosswind	-67.09	23.12	24.71
	Upwind	-66.65	9.72	25.46
HV	Downwind	-68.74	14.17	24.47
	Crosswind	-73.09	14.85	26.66
	Upwind	-50.18	12.41	25.15
VV	Downwind	-50.16	12.30	23.92
	Crosswind	-52.60	12.30	22.09

2.2.3   Clutter to noise ratio

To demonstrate the modelling of these parameters, the CNR has been calculated using parameters representative of the F35 flight with the mean backscatter determined from the IRSG model. Figure 3 shows the result which demonstrates a good match with appropriate variation in both azimuth and grazing.

2.3   Probability distributions

Statistical models of the PDF are used to model the spread of received backscatter values. A number of them have been used to model sea-clutter in the past with varying degrees of success [Dong 2006, Rosenberg, Crisp & Stacy 2010*b*, Weinberg 2011*a*, Rosenberg & Bocquet 2015,
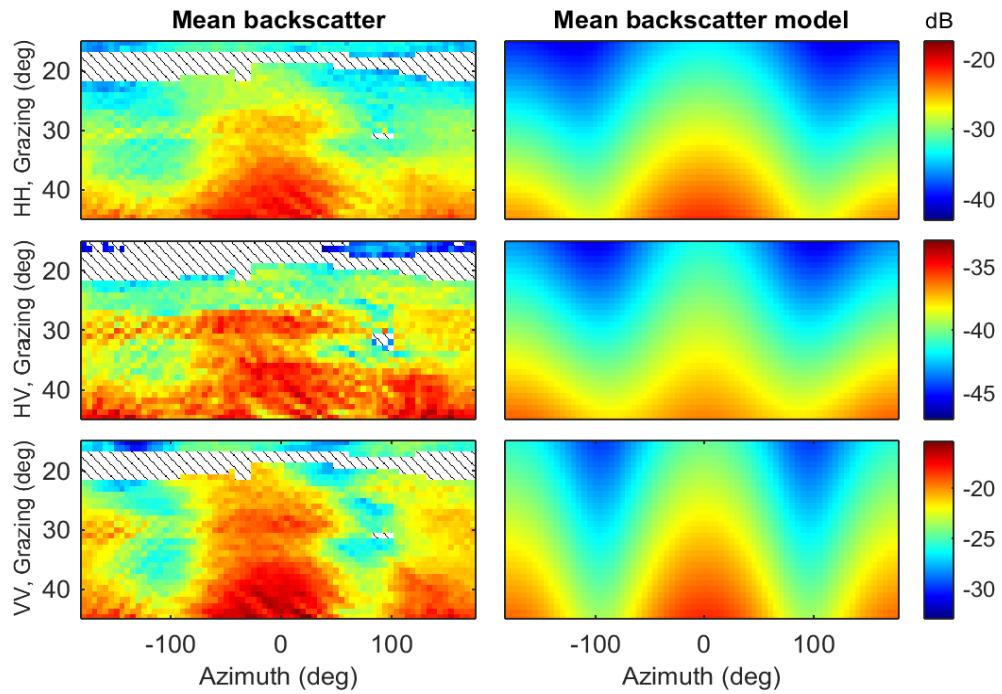
Figure 2: *Mean backscatter comparison with varying azimuth and grazing using the IRSG model, left - Ingara F35 data, right - model output with wind speed, $U = 10.3$ m/s.*
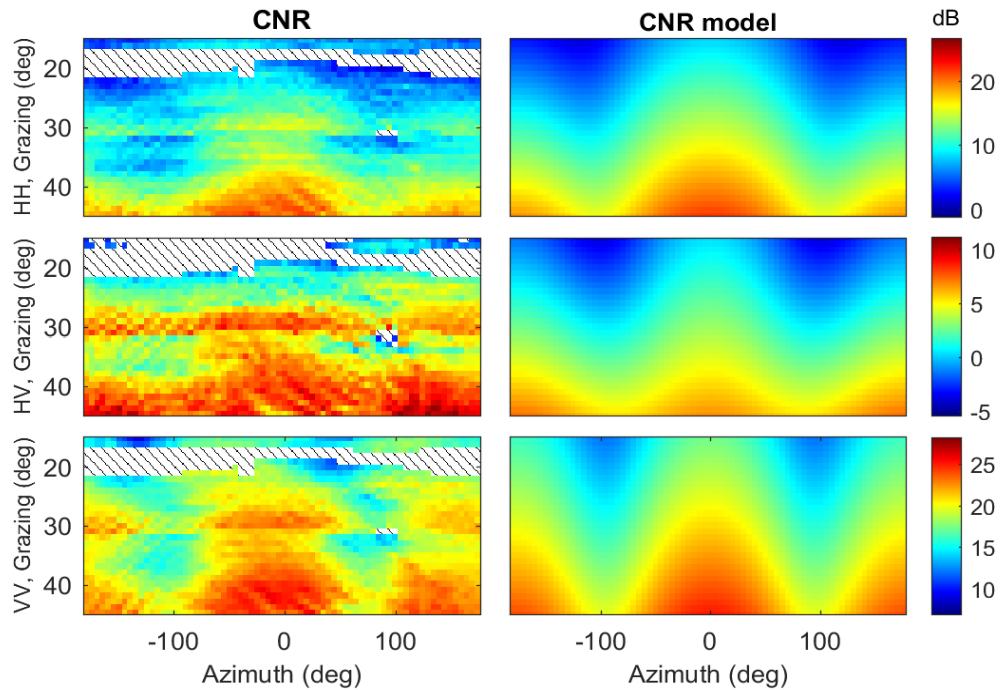

Figure 3: *CNR comparison with varying azimuth and grazing: left - Ingara F35 data, right - model using parameters matched to data and mean backscatter determined from the IRSG model.*

Rosenberg, Watts & Bocquet 2014]. The first model considered is the K-distribution which is used to characterise the bulk of the PDF. To understand the development of the K-distribution, consider a radar receiving in-phase and quadrature data from an external clutter source with its amplitude defined by Gaussian statistics with zero mean and variance, x. In addition, thermal noise from within the radar will add a component p_n which is included by offsetting the variance x. The PDF of the clutter and noise is then given by,

$$P_E(E|x,p_n) = \frac{1}{\sqrt{2\pi(x+p_n)}} \exp\left[-\frac{E^2}{2(x+p_n)}\right] \tag{12}$$

with the envelope of these components, $y = \sqrt{E_{ip}^2 + E_{quad}^2}$, then determined by a Rayleigh PDF,

$$P_y(y|x,p_n) = \frac{y}{x+p_n} \exp\left[-\frac{y^2}{2(x+p_n)}\right]. \tag{13}$$

In the target detection analysis, the received pulses are often converted to power (square law), $z = y^2$ and then summed to improve detection performance. Consider the sum of M exponential random variables,

$$Z = \sum_{m=1}^{M} z_m. \tag{14}$$

If the returns from successive pulses are uncorrelated, the received power is then described by a gamma PDF,

$$P_{Z|x}(Z|x) = \frac{Z^{M-1}}{(x+p_n)^M \Gamma(M)} \exp\left[-\frac{Z}{x+p_n}\right]. \tag{15}$$

2.3.1 Compound distributions

The distribution in Equation 15 models the speckle component of the sea-clutter. To include the texture component which modulates the speckle, a compound distribution can be used,

$$P(Z) = \int_0^\infty P_{Z|x}(Z|x)P_x(x)dx \tag{16}$$

where $P_x(x)$ is the distribution of the texture component. To achieve a K-distribution, the texture is also gamma distributed

$$P_x(x) = \frac{b^\nu}{\Gamma(\nu)} x^{\nu-1} \exp\left[-bx\right], \quad \nu, b > 0 \tag{17}$$

with shape given by ν and scale, $b = \nu/p_c$ related to the mean power, p_c. For the Pareto distribution, the texture has an inverse gamma distribution

$$P_x(x) = \frac{c^a}{\Gamma(a)} x^{-a-1} \exp\left[-c/x\right], \quad a > 1, c > 0 \tag{18}$$

where a is the shape and $c = p_c(a-1)$ is the scale. In general, numerical integration is required to evaluate the compound distributions. However, if thermal noise is not present ($p_n = 0$), analytic

forms of the distributions can be derived. With a gamma distributed texture, the K-distribution is obtained,

$$P(Z) = \frac{2}{Z} \left(bZ\right)^{\frac{M+\nu}{2}} \frac{1}{\Gamma(M)\Gamma(\nu)} K_{\nu-M}\left(2\sqrt{bZ}\right) \tag{19}$$

where $K_{\nu-M}(\cdot)$ is the modified Bessel function of the second kind with order $\nu - M$. If the texture is inverse gamma distributed, the general solution is a compound gamma distribution

$$P(Z) = \frac{Z^{M-1}c^a\Gamma(M+a)}{(c+Z)^{M+a}\Gamma(M)\Gamma(a)}, \qquad a > 1, c > 0 \tag{20}$$

which reduces to the generalised Pareto type II or Lomax distribution for $M = 1$,

$$P(Z) = \frac{ac^a}{(c+Z)^{1+a}}. \tag{21}$$

The result in Figure 4 shows the time domain PDF and the complementary cumulative distribution function (CCDF) for the F35 dataset (in intensity) with the Pareto distribution fit overlaid in black. For comparison, the equivalent fit for the K distribution is shown in red and is clearly under-fitting the data, particularly in the HH channel. Thermal noise is assumed for both models with the recently published $z \log z$ shape estimation method used to estimate the shape values [Bocquet 2015].
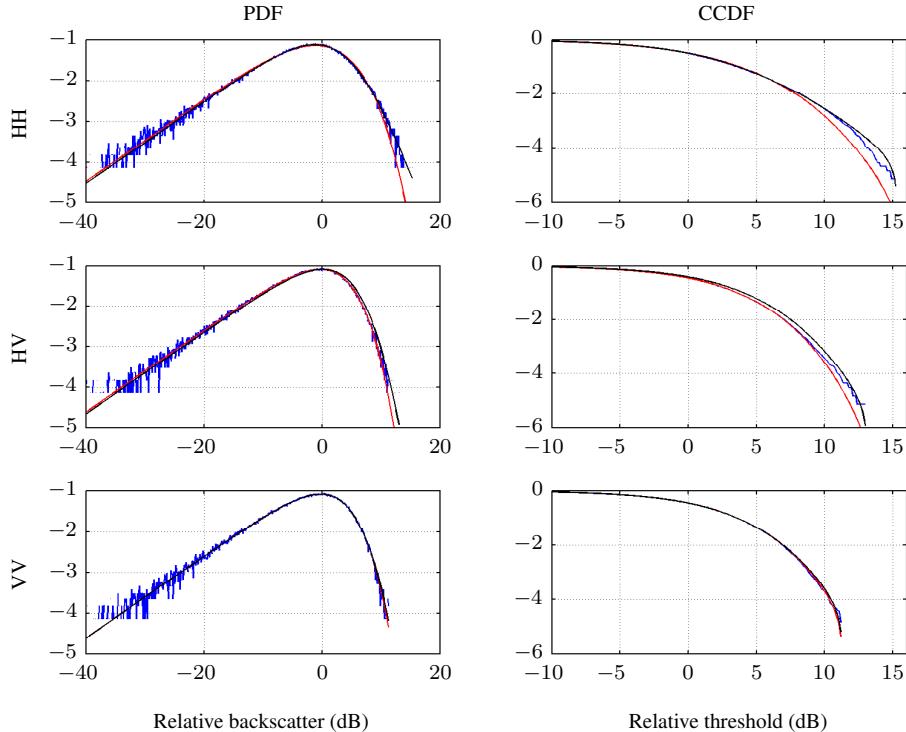

Figure 4: *Time domain intensity distributions - upwind* 30° *grazing. Data in blue, K-distribution fit in red, Pareto distribution fit in black.*

2.3.2 Shape model

Until recently, the only model suitable for modelling the K-distribution shape was for low grazing angles [Ward, Tough & Watts 2013]. Using the Ingara data set, there have now been three iterations of models designed to model the shape at medium grazing angles with all three applied separately to each polarisation. The first was designed to model only the geometry for an individual day [Rosenberg, Crisp & Stacy 2009]. This was then extended by Crisp, Rosenberg & Stacy [2015] to include extra components for the environmental conditions and resolution. These are combined into a global model comprising 24 coefficients at the finest resolution (0.75 m range $\times$ 63 m azimuth). The third iteration is a variation designed to better model other parameters of interest which have a stronger component due to the swell [Rosenberg et al. 2015]. It was also applied to model the Pareto shape and offers a slightly better fit to the estimated K-distribution shape. Consequently, this third iteration is used in the report. The validity of the model parameter bounds are determined by the input data. This includes a CPI of 64 pulses, a resolution of 0.75 m range $\times$ 63 m azimuth, all azimuth angles and linear polarisations, sea-states 2-6 and grazing angles from $15° - 45°$.

If X is a generic parameter to be modelled, then the geometric relationship can be written as the weighted sum of two components which represent the wind and swell directions. Assuming the data has been rotated so upwind is now at $0°$,

$$X(\theta, \phi) = a_0'\theta^\gamma \left[1 + a_1'\cos\phi + a_2'\cos(2\phi) + a_3'\cos(\phi - \psi) + a_4'\cos(2(\phi - \psi))\right] \quad (22)$$

where ψ is the swell direction relative to upwind and $\gamma, a_0', \ldots, a_4'$ are the model coefficients. Representing the ocean conditions is difficult and the shape model uses only the wind speed and the significant wave height $H_{1/3}$,

$$Y = b_0' + b_1'\log_{10}(U) + b_2'H_{1/3} \quad (23)$$

where b_0', b_1', b_2' are the model coefficients. To relate these two models, the coefficients in Equation 22 must be altered so they are independent of grazing angle. This is achieved by introducing a normalisation factor, θ_0 and then redefining Equation 22 as

$$X(\theta, \phi) = \left(\frac{\theta}{\theta_0}\right)^\gamma \left[\alpha_0 + \alpha_1\cos\phi + \alpha_2\cos(2\phi) + \alpha_3\cos(\phi - \psi) + a_4\cos(2(\phi - \psi))\right] \quad (24)$$

where the new coefficients are related by

$$\alpha_0 = a_0'\theta_0^\gamma, \quad \alpha_1 = a_0'a_1'\theta_0^\gamma, \quad \ldots, \quad \alpha_4 = a_0'a_4'\theta_0^\gamma. \quad (25)$$

Implementing the model involves matching γ and each of the α coefficients to Equation 23. This in turn requires 6 sets of the b' parameters or 18 coefficients in total for each polarisation. These model coefficients for K and Pareto distributions are presented in Table 4. Once the new coefficients in Equation 25 are evaluated, they can be substituted into Equation 24 with the normalising grazing angle θ_0 set to $30°$ to derive the final model value.

Finally, it has been observed that shape values less than 2 can result in bad fits to the Ingara data. To enforce this lower bound with the new shape model, the model coefficients have been derived for a modified shape, $a - 2$, with the final shape value then increased by 2 to compensate. Figure 5 shows the variation of the Pareto shape over grazing and azimuth for the F35 run with a model created with the same input parameters. Clearly, the model captures the main trends quite well. These include a include a linear increase with grazing and sinusoidal variation in azimuth with a peak in the upwind and downwind directions.
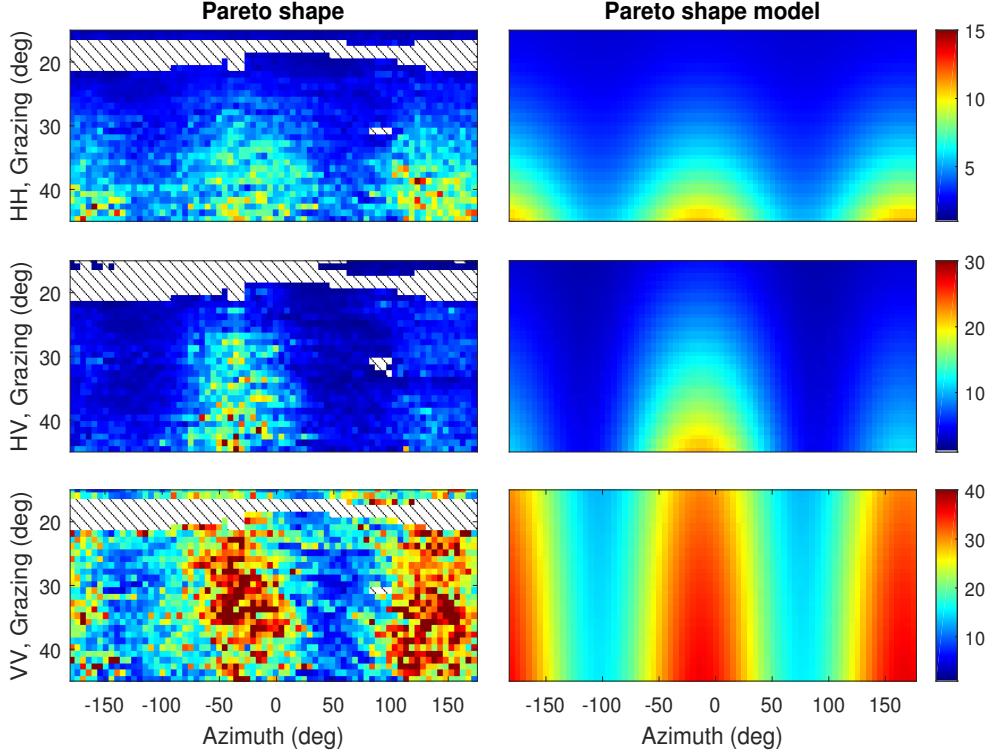
Figure 5: Pareto shape parameter model comparison with varying azimuth and grazing: left - shape estimated from F35 data set, right - model output with wind speed, U = 10.3 m/s, significant wave height, $H_{1/3}$ = 2.6 m, wind swell angle, $\psi = 0°$.

2.4 Temporal correlation

To accurately capture the correlation due to the speckle, platform motion and antenna scanning, a model is required which relates both the sea conditions and the relevant radar parameters. In the following sections, different Gaussian models are used to model each of the components in the frequency domain with their overall spread spectrum given as their convolution:

$$C(f) = \frac{1}{\sigma\sqrt{2\pi}} \exp\left(-\frac{(f-f_0)^2}{2\sigma^2}\right) \tag{26}$$

where f_0 is the mean and the total variance is the sum of the component variances,

$$\sigma^2 = \sigma_s^2 + \sigma_{pm}^2 + \sigma_{scan}^2. \tag{27}$$

The combined temporal auto-correlation function (ACF) is then found by taking the Fourier transform

$$C(t) = \exp(-j2\pi f_0 t) \exp\left(-\frac{t^2}{T'^2}\right) \tag{28}$$

with the overall decorrelation time given by

$$T' = \frac{1}{\sqrt{2\pi}\sigma}. \tag{29}$$

Table 4: K and Pareto distribution shape coefficients.

		K shape			Pareto shape		
		b_0'	b_1'	b_2'	b_0'	b_1'	b_2'
HH	γ	11.52	-8.72	-0.11	13.4	-10.15	-0.064
	α_0	-1.37	4.18	-0.078	-0.93	3.00	-0.11
	α_1	-0.38	0.11	0.050	-0.39	0.15	0.065
	α_2	-0.14	0.80	0.024	-0.31	0.89	-0.028
	α_3	-0.018	-0.19	0.043	0.32	-0.49	0.050
	α_4	-0.51	0.68	0.019	-0.62	1.01	0.00037
HV	γ	4.83	-3.33	0.054	8.34	-6.64	0.061
	α_0	-5.78	11.52	-0.39	-5.68	10.75	-0.40
	α_1	-4.17	6.38	-0.24	-3.55	5.36	-0.21
	α_2	-0.89	3.32	-0.033	-0.52	2.72	-0.21
	α_3	1.98	-2.59	-0.030	2.96	-4.35	0.080
	α_4	-0.16	0.12	0.40	0.41	0.48	0.22
VV	γ	0.28	-0.38	0.11	0.28	-0.39	0.11
	α_0	14.06	19.11	-4.06	13.43	18.78	-4.06
	α_1	-6.00	3.80	0.60	-7.37	5.61	0.64
	α_2	0.93	8.25	-0.80	1.41	7.29	-1.03
	α_3	-0.72	0.15	0.16	2.47	-2.49	0.095
	α_4	-3.91	5.56	0.40	-10.87	16.67	-0.41

2.4.1 Clutter width

As the sea state becomes greater, the wind speed, wave height, wave length and the Doppler bandwidth all increase. Regarding the latter, Hicks et al. [1960] have shown experimentally that the Doppler spread at high grazing angles is proportional to the wave height divided by the wave period. Previous analysis of the bi-modal Doppler spectrum [Rosenberg 2014] found only minor trends in azimuth and grazing angle and hence the model is only a function of wind speed and wave height. The model represents the temporal decorrelation which is measured at the point where the absolute value of the ACF decays to $1/e$. It is described by three sets of coefficients, one for each polarisation. Note that this model only considers the real part of the correlation and hence assumes that the Doppler spectrum is centred at 0 Hz. The model is given by

$$T = (p_0 + p_1 U + p_2 H_{1/3}) \times 10^{-3} \tag{30}$$

with the model coefficients given in Table 5. Figure 6 shows the model fit for the two component model where the trend is that the mean decorrelation times are longer when the wind speed and wave height are smaller. The RMS errors for the HH and VV channels are 1.1 and 0.74 ms respectively. The HV decorrelation time is modelled as the average of the HH and VV model outputs.

A Gaussian model can then be used to represent the correlation,

$$A(t) = \exp\left[-\frac{t^2}{T^2}\right], \tag{31}$$

Table 5: *Decorrelation model parameters*

	HH	VV
p_0	16.67	17.13
p_1	-0.68	-0.40
p_2	-0.87	-0.91
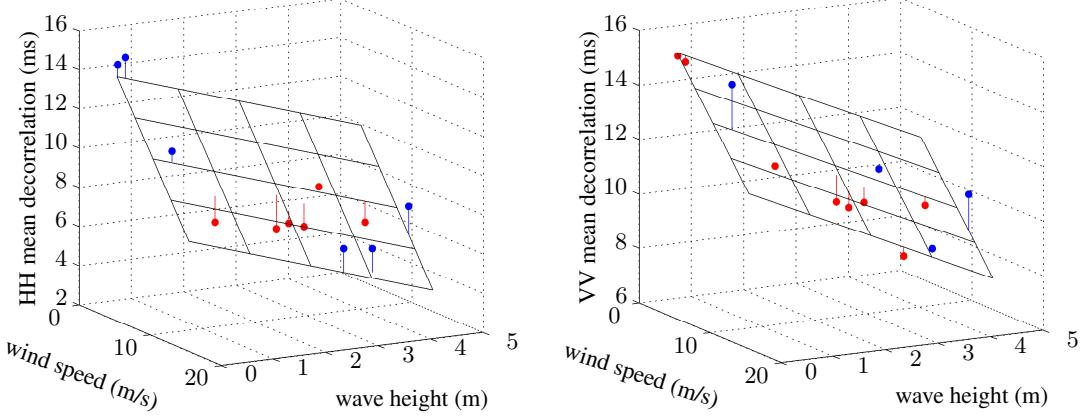
Figure 6: *Mean temporal decorrelation as a function of wind speed and wave height. Left - HH, Right - VV.*

with the spectrum found by taking a Fourier transform

$$
\begin{aligned}
A(f) &= \sqrt{\pi} T \exp\left(-\pi^2 f^2 T^2\right) \\
&= \frac{1}{\sigma_{\mathrm{s}}\sqrt{2\pi}} \exp\left(-\frac{f^2}{2\sigma_{\mathrm{s}}^2}\right)
\end{aligned}
\tag{32}
$$

where $\sigma_{\mathrm{s}} = 1/(\sqrt{2}\pi T)$.

2.4.2 Platform motion

Antenna beampatterns are typically defined in an angular domain with specifications for the minimum sidelobe level and two-way 3 dB azimuth beam width. To simplify the modelling, we will assume a Gaussian beam pattern with azimuth angle, ϕ_0,

$$
G(\phi_0) = \exp\left[-\frac{\phi_0^2}{(2\ln 2)\phi_{3\mathrm{dB}}^2}\right].
\tag{33}
$$

Assuming that the elevation beam pattern does not change significantly over the clutter patch, the Doppler frequency can be related to the beam pattern by

$$
f \approx \frac{2v_p\phi_0|\sin\phi_{\mathrm{b}}|\cos\theta_{\mathrm{el}}}{\lambda}
\tag{34}
$$

where ϕ_{b} is the antenna azimuth direction relative to the platform velocity and θ_{el} is the elevation angle. The azimuth angle can then be related to the Doppler frequency and hence the platform

velocity by substituting

$$\phi_0 = \frac{f\lambda}{2v_p|\sin\phi_{\mathrm{b}}|\cos\theta_{\mathrm{el}}} \tag{35}$$

into Equation 33, giving

$$G(f) \approx \exp\left(-\frac{f^2}{2\sigma_{\mathrm{pm}}^2}\right) \tag{36}$$

where

$$\sigma_{\mathrm{pm}} = \frac{1}{\sqrt{2\ln 2}}\frac{v_p|\sin\phi_{\mathrm{b}}|\phi_{\mathrm{3dB}}\cos\theta_{\mathrm{el}}}{\lambda}$$
$$\approx 0.85\frac{v_p|\sin\phi_{\mathrm{b}}|\phi_{\mathrm{3dB}}\cos\theta_{\mathrm{el}}}{\lambda}. \tag{37}$$

2.4.3 Antenna scanning

Although the Ingara radar did not scan during the sea-clutter collections, antenna scanning can be modelled using the relationship in Skolnik [2008],

$$\sigma_{\mathrm{scan}} = \frac{\sqrt{2\ln 2}}{2\pi}\frac{\phi_{\mathrm{scan}}}{\phi_{3dB}}$$
$$\approx 0.19\frac{\phi_{\mathrm{scan}}}{\phi_{3dB}} \tag{38}$$

where ϕ_{scan} is the antenna rotation rate in rad/s.

3 Detection probability framework

The problem of target detection is commonly presented with two hypotheses, H_0 - clutter plus noise is present in the radar return and H_1 - a target is present with the clutter and noise. Figure 7 shows the case for non-coherent detection where two histograms are shown which correspond to these hypotheses. The premise of target detection is to select an acceptable probability of false alarm, P_{fa} and determine the threshold, Y based on the clutter plus noise model. Any backscatter response above the threshold is then declared a potential target. If a detector can measure or estimate the clutter distribution parameters and set the corresponding threshold, then the detector can be considered CFAR. The P_{fa} and the probability of detection, P_{d} can be defined as

$$P_{\text{fa}}(Y) = \text{Prob}(Z > Y|H_0) = \int_Y^\infty P_{\text{c}}(Z)dZ \tag{39}$$

$$P_{\text{d}}(Y) = \text{Prob}(Z > Y|H_1) = \int_Y^\infty P_{\text{t}}(Z)dZ \tag{40}$$

where $P_{\text{c}}(Z)$ represents the clutter plus noise PDF and $P_{\text{t}}(Z)$ the target plus clutter and noise PDF. Also in this figure, P_{m} denotes the miss probability.
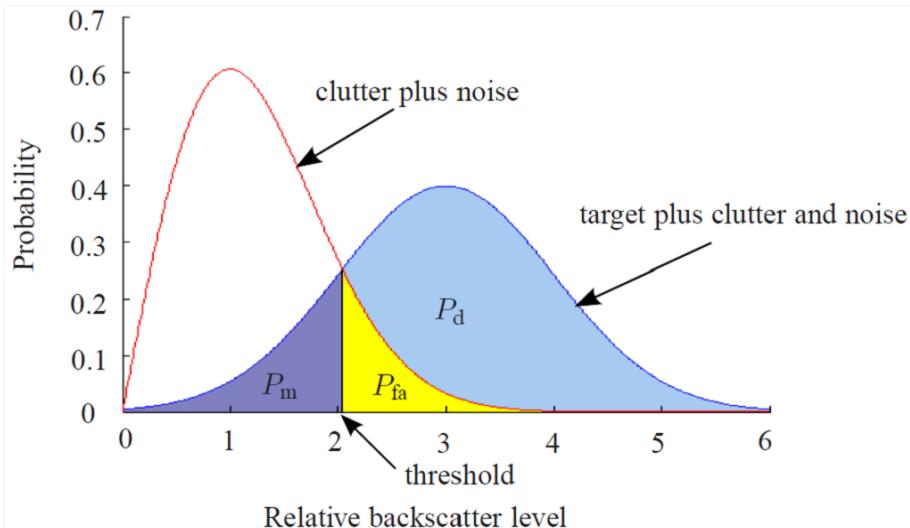
Figure 7: Detection probabilities showing distributions for the clutter plus noise and the target plus clutter and noise. The threshold determines the three regions: P_m, P_{fa} and P_d.

The theory of optimal target detection is well summarised in Ward, Tough & Watts [2013, Chapter 10]. The principle of finding an optimal P_{d} for a fixed P_{fa} is known as the Neyman-Pearson criterion and can be written as the ratio of the interference and target plus interference PDFs

$$\Lambda(z) = \frac{P_{\text{c}}(Z)}{P_{\text{t}}(Z)} > Y. \tag{41}$$

Expressions for compound PDFs are generally quite complex, particularly when correlation is included and the signals are treated coherently. Also CFAR control remains difficult when estimates of the covariance are required and the sea-clutter is non-stationary. This has led to non-coherent schemes which are often sub-optimal and may or may not be CFAR. These

practical detectors are typically easier to compute and require adjustment of the threshold to maintain a constant false alarm rate. Some of the latter include the cell-averaging, single-sided and ordered statistic CFAR [Ward, Tough & Watts 2013, Chapter 13]. This report only considers detection with a constant or fixed threshold and with non-coherent integration as the mathematics are more tractable. We assume that a threshold is applied after pulse-to-pulse integration and there is a CFAR system to adjust the threshold for a specified P_{fa}. The exact analytic expressions then represent the performance results which would be expected if the clutter parameters are known and are useful as a benchmark for other detection approaches.

This section provides details of the P_{fa} and P_{d} calculations for a target present in clutter and noise (interference). The first Sections 3.1-3.2 assume that the clutter and target distributions are uncorrelated, such as would be the case in a sufficiently frequency agile radar. Section 3.1 considers a constant target present in Gaussian interference covering a 'local area'. The solution for the P_{d} is known as a Marcum model and was first described by Marcum [1960]. However, the RCS of a target will typically fluctuate and Section 3.2 describes a method for representing this fluctuation in terms of generalised Weinstock fluctuations, [Weinstock 1964] and Swerling models, [Swerling 1960].

Some level of temporal correlation will typically be present on both the target and the speckle component of the clutter. For the former, it is commonly assumed to be either totally correlated or uncorrelated and fluctuate around a mean level with an exponential distribution (Swerling cases 1 and 2) or chi-squared distribution (cases 3 and 4). However, an early study by Edrington [1965] found that radar echoes from a number of aircraft were in the fact partially correlated and that performance prediction models needed to be modified. Barton [1969] looked at the target correlation and calculated an effective number of independent looks based on the correlation time relative to the total observation time. With this approach, the P_{d} can then be determined using the traditional solution for totally correlated targets. A subsequent study by Kanter [1986] then derived the exact P_{d} for exponential fluctuating targets rather than with an effective number of looks. Weiner [1988] then did the same for chi-squared fluctuating targets.

Regarding the speckle component, there are a number of approaches in the literature which can be used to account for different levels of correlation. Ideally, an approach should be able to model the ACF through its representation of the Doppler spectrum of the received signal, which is related through a Fourier transform. The simplest method was presented by Farina et al. [1996] and is based on an improvement factor which can be used to modify the required SIR in the P_{d} calculation. However, it assumes a Gaussian Doppler spectrum and hence cannot be used to model more complex spectra with components due to breaking waves and discrete spikes. A second approach which is only suitable for exponential fluctuating targets was presented by Hou & Morinaga [1988]. This result allows both partially correlated targets and speckle with exact representations of their ACF's, but suffers from numerical instabilities and is not generalised for all Swerling target models. The final approach from the literature by Ward, Tough & Watts [2013] (WTW) treats the speckle, thermal noise and target separately. By using an estimate of the 'effective' number of looks for the speckle, it can overcome the numerical problems of Hu and Morinaga. While this method is useful, it becomes very computationally intensive as the CNR gets higher and fails completely when there is only clutter present. This led to a modification by Rosenberg & Bocquet [2013b] which overcomes this limitation by allowing any positive number of looks for either the speckle or target. Thermal noise has also been included in this formulation, with the caveat that it will be correlated with the speckle and is therefore not as accurate at low CNR. A tradeoff is therefore proposed, where the WTW method is used for low CNR and the

modification used for larger CNR. These algorithms are described in Section 3.3 with the last Section 3.4 outlining how the models can be extended to a compound representation where the local area is now augmented by a 'global' fluctuation. This 'texture' is assumed to be uncorrelated and hence the results presented here may not be completely accurate for scan-to-scan radars where a longer time between looks may result in a variation of the texture.

3.1 Detection with a constant target

The first model represents a target with a non-fluctuating or constant RCS present in Gaussian interference and is known as a Marcum model or Swerling case 0. In the intensity domain, the PDF for a single pulse is given by a Rice distribution, [Ward, Tough & Watts 2013],

$$P(z|x, p_n, A) = \frac{1}{x + p_n} \exp\left(-\frac{z + A^2}{x + p_n}\right) I_0\left(\frac{2A\sqrt{z}}{x + p_n}\right) \tag{42}$$

where the target power is given by A^2 and $I_0(\cdot)$ is a modified Bessel function of the first kind, order 0. For the following derivations, it is useful to define the local received signal and the target power as being normalised to the interference power (i.e. the local SIR),

$$\mu = \frac{1}{x + p_n} \sum_{m=1}^{M} z_m, \tag{43}$$

$$s = \frac{1}{x + p_n} \sum_{m=1}^{M} A_m^2. \tag{44}$$

where x and p_n are the speckle and thermal noise means and M is the number of looks or non-coherent averages. The PDF describing the interference is then given by,

$$P(\mu) = \frac{\mu^{M-1}}{\Gamma(M)} e^{-\mu} \tag{45}$$

and the P_{fa} can be determined by calculating

$$\begin{aligned} P_{\text{fa}}(\tau|M) &= \int_{\tau}^{\infty} P(\mu) d\mu \\ &= \frac{\Gamma(M, \tau)}{\Gamma(M)} \end{aligned} \tag{46}$$

where τ is the normalised threshold related to the 'true' threshold Y

$$\tau = \frac{Y}{x + p_n} \tag{47}$$

and $\Gamma(M) = (M - 1)!$ and $\Gamma(M, \tau)$ is the upper incomplete gamma function which can be evaluated for integer M using the following series [Gradshteyn & Ryzhik 1994, §3.351/2 and §8.352/2]:

$$\begin{aligned} \Gamma(M, \tau) &= \int_{\tau}^{\infty} \mu^{M-1} e^{-\mu} d\mu \\ &= \Gamma(M) e^{-\tau} \sum_{k=0}^{M-1} \frac{\tau^k}{k!}. \end{aligned} \tag{48}$$

For the total received signal, the PDF becomes a multi-look Rice distribution,

$$
\begin{aligned}
P(\mu|s, M) &= \left(\frac{\mu}{s}\right)^{(M-1)/2} \exp\left(-(\mu + s)\right) I_{M-1}\left(2\sqrt{\mu s}\right) \\
&= e^{-(\mu+s)} \left(\frac{\mu}{s}\right)^{(M-1)/2} \sum_{k=0}^{\infty} \frac{1}{k!\Gamma(M+k)} (\mu s)^{(M-1+2k)/2} \\
&= e^{-(\mu+s)} \sum_{k=0}^{\infty} \frac{1}{k!\Gamma(M+k)} \mu^{M-1+k} s^k \\
&= \sum_{k=0}^{\infty} \frac{e^{-\mu}\mu^{M+k-1}}{(M+k-1)!} \frac{e^{-s}s^k}{k!}
\end{aligned}
\tag{49}
$$

where the Bessel function is expanded using the series [Gradshteyn & Ryzhik 1994, §8.445]:

$$
I_L(z) = \sum_{k=0}^{\infty} \frac{1}{k!\Gamma(L+k+1)} \left(\frac{z}{2}\right)^{L+2k}.
\tag{50}
$$

If the SIR for a constant target is given by

$$
S = \frac{M\left\langle A^2 \right\rangle}{x + p_n}
\tag{51}
$$

where $\langle\cdot\rangle$ denotes the expectation. If K denotes the fluctuation parameter of a chi-squared distributed target presented below, then the probability of detection for a constant target, $P_{\mathrm{d},K}$ (where $K \to \infty$) can be given in terms of the normalised threshold τ with $s = S$,

$$
\begin{aligned}
P_{\mathrm{d},\infty}(\tau|S, M) &= \int_{\tau}^{\infty} P(\mu|S, M)d\mu \\
&= \sum_{k=0}^{\infty} \frac{e^{-S}S^k}{k!} \frac{1}{(M+k-1)!} \int_{\tau}^{\infty} e^{-\mu}\mu^{M+k-1}d\mu \\
&= \sum_{k=0}^{\infty} \frac{e^{-S}S^k}{k!} e^{-\tau} \sum_{m=0}^{M+k-1} \frac{\tau^m}{m!} \\
&= \sum_{k=0}^{\infty} \frac{e^{-S}S^k}{k!} e^{-\tau} \left(\sum_{m=0}^{M-1} \frac{\tau^m}{m!} + \sum_{m=M}^{M+k-1} \frac{\tau^m}{m!} \right) \\
&= \sum_{k=0}^{M-1} e^{-\tau}\frac{\tau^k}{k!} + \sum_{k=0}^{\infty} \frac{e^{-S}S^k}{k!} \sum_{m=M}^{M+k-1} e^{-\tau}\frac{\tau^m}{m!} \\
&= \sum_{k=0}^{M-1} e^{-\tau}\frac{\tau^k}{k!} + \sum_{k=M}^{\infty} e^{-\tau}\frac{\tau^k}{k!} \left(1 - \sum_{m=0}^{k-M} \frac{e^{-S}S^m}{m!} \right)
\end{aligned}
\tag{52}
$$

where the relationship in Equation 48 was used to evaluate the integral and the manipulation of the series makes use of the identity

$$
\sum_{k=0}^{\infty} \frac{e^{-\tau}\tau^k}{k!} = 1.
\tag{53}
$$

The series in Equation 52 is difficult to evaluate, but effective methods were devised by Shnidman [Shnidman 1976, Shnidman 1989]. $P_{d,\infty}$ can also be expressed in terms of the generalised Marcum Q-function [Shnidman 1976],

$$P_{d,\infty}(\tau|S, M) = Q_M \left(\sqrt{2MS}, \sqrt{2\tau} \right) \tag{54}$$

where

$$Q_M(m, n) = \frac{1}{m^{M-1}} \int_n^\infty \mu^M \exp\left(-\frac{\mu^2 + m^2}{2} \right) I_{M-1}(m\mu)d\mu. \tag{55}$$

The solution for the P_{fa} in Equation 46 can be recovered by setting $S = 0$ in Equation 52. For most radar targets of interest however, the target reflection will not be constant. The following section looks at a generalisation of this model.

3.2   Detection with a fluctuating target

A target will typically fluctuate over the integration period and from scan to scan (different integration periods). Shnidman [1995] describes four different fluctuation models including chi-square, log-normal, Weibull and Ricean distributions. The chi-square distribution is the most popular however as it can be used to represent the well known Swerling models. With this model, the target fluctuation with parameter K is given by

$$P(s|S, K) = \frac{s^{K-1}}{\Gamma(K)} \left(\frac{K}{S} \right)^K \exp\left(-\frac{Ks}{S} \right). \tag{56}$$

To include this in the probability of detection calculation, it is multiplied with the target plus noise PDF and then the product is integrated over the random variable s,

$$P_{d,K}(\tau|S, M) = \int_0^\infty P(s|S, K) \int_\tau^\infty P(\mu|s, M)d\mu ds$$
$$= \int_0^\infty P(s|S, K)P_{d,\infty}(\tau|s, M)ds. \tag{57}$$

A general solution is given by Shnidman [1995],

$$P_{d,K}(\tau|S, M) = \sum_{m=0}^{M-1} e^{-\tau}\frac{\tau^m}{m!} + \sum_{m=M}^\infty e^{-\tau}\frac{\tau^m}{m!}$$
$$\times \left[1 - \sum_{n=0}^{m-M} \frac{\Gamma(K+n)}{n!\Gamma(k)} \left(\frac{1}{1+S/K} \right)^K \left(\frac{S/K}{1+S/K} \right)^n \right] \tag{58}$$

where the P_{fa} is identical to the non-fluctuating target case. This series is also difficult to evaluate, but an effective method is given by Shnidman [1995].

There are also a number of special cases depending on the choice of the parameter K. For example, when $K \to \infty$ this equation reverts back to the constant target case from the previous section. Other studies have looked at the region where $0 \leq K \leq 1$, where the models are known as Weinstock fluctuations, [Weinstock 1964]. These represent slowly fluctuating targets and have been shown to accurately model the fluctuation from objects which are cylindrical in shape. Four

other special cases of this model are when $K = 1$, M, 2 and $2M$. These are known as the Swerling models 1-4 and were originally proposed by [Swerling 1960] and detailed in the books by [Meyer & Mayer 1973, Briggs 2004]. These models are able to capture the majority of target RCS fluctuations and are popular due to their physical interpretation, either representing the target fluctuation pulse to pulse or scan to scan, [Allen & Urkowitz 1993].

Examples of the four Swerling models are shown in Figure 8 for three values of the SIR. Cases 1 and 3 are clearly more spread out due to the larger number of scatterers being observed over the slower observation time. Conversely, cases 2 and 4 have narrower distributions due to the faster change of RCS. As the SIR increases, the distribution becomes more spread and shifts to the right.
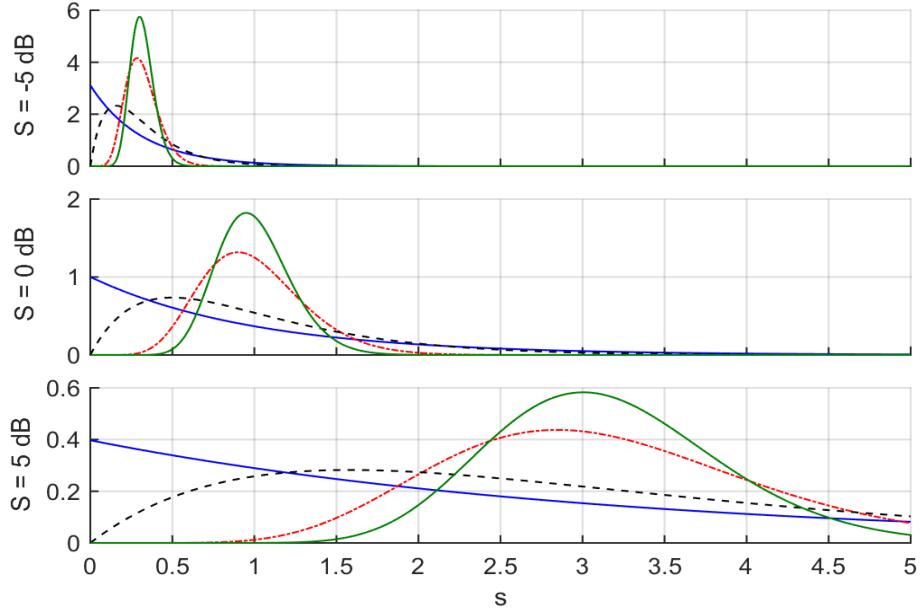
Figure 8: Swerling model comparison for three different values of SIR: (—) case 1,(-.-) case 2, (- -) case 3, (—) case 4, top: $S = -5$ dB, middle: $S = 0$ dB, bottom: $S = 5$ dB.

Swerling model - case 1, $(K = 1)$

The first two Swerling cases relate to targets with an exponential fluctuation. They represent several independently fluctuating reflectors of approximately equal area. This would apply to objects which are large compared to the radar wavelength (and not shaped too much like a sphere), [Swerling 1960]. For the first case, a constant RCS is assumed during a single scan (group of pulses) with changes from scan to scan. It is suitable for modelling targets viewed with a high PRF and scan rate. The P_d solution is given by,

$$
P_{\mathrm{d},1}(\tau|S, M) = \frac{\Gamma(M-1, \tau)}{\Gamma(M-1)} + \left(1 + \frac{1}{S}\right)^{M-1}
$$
$$
\times \left(1 - \Gamma\left(M-1, \frac{\tau}{1 + (1/S)}\right) / \Gamma(M-1)\right) \exp\left(-\frac{\tau}{1+S}\right). \tag{59}
$$

Swerling model - case 2, $(K = M)$

The Swerling case 2 also assumes the targets have an exponential fluctuation, but now with independent fluctuations from pulse to pulse. It is suited to scenarios where targets are viewed with a low PRF or when small changes in orientation cause significant changes in the illuminated area. The latter can arise from reflections from a long thin object subjected to a high frequency signal, [Meyer & Mayer 1973]. For this case, the P_d solution is given by,

$$P_{\mathrm{d},M}(\tau|S,M) = 1 - \Gamma\left(M, \frac{\tau}{1+S/M}\right)/\Gamma(M). \tag{60}$$

Swerling model - case 3, $(K = 2)$

The target models defined by cases 3 and 4 represent a chi-square distribution with 4 degrees of freedom and hence there is not as much randomness as the first two cases. The model effectively represents one large reflector combined with a number of small reflectors or just one large reflector subject to small changes in orientation. Case 3 represents a target with constant RCS during a single scan with changes from scan to scan. The P_d solution is given by,

$$P_{\mathrm{d},2}(\tau|S,M) = \begin{cases} \dfrac{\exp(-C\tau)}{(1-C)^{M-2}}\left(1 - \dfrac{(M-2)C}{(1-C)} + C\tau\right), & M \le 2 \\[2ex] \dfrac{\Gamma(M-1,\tau)}{\Gamma(M-1)} + \dfrac{\tau^{M-1}e^{-C\tau}C}{(M-2)!} + \dfrac{e^{-C\tau}}{(1-C)^{M-2}} \\[2ex] \quad \times \left(1 - \dfrac{(M-2)C}{(1-C)} + C\tau\right)\left(1 - \dfrac{\Gamma(M-1,\tau(1-C))}{\Gamma(M-1)}\right), & \text{otherwise} \end{cases}$$

where

$$C = \frac{1}{1+S/2}. \tag{61}$$

Swerling model - case 4, $(K = 2M)$

This case is similar to the previous but now represents a target with independent fluctuations from pulse to pulse. The P_d solution is given by,

$$P_{\mathrm{d},2M}(\tau|S,M) = D^N \sum_{k=0}^{M} \frac{M!}{k!(M-k)!}\left(\frac{1-D}{D}\right)^{M-k} \frac{\Gamma(2M-k,D\tau)}{\Gamma(2M-k)} \tag{62}$$

where

$$D = \frac{1}{1+S/(2M)}. \tag{63}$$

3.3 Detection in correlated clutter

In many radar systems, there will be correlation between pulses. There have been a number of different attempts to model the correlation of both the clutter and the target, but by far the most useful is the method by Ward, Tough & Watts [2013, Section 12.4] (WTW). The technique accounts for the correlation by defining $1 \leq L \leq M$ as a measure of the effective number of independent clutter samples. L is not necessarily an integer, and ranges from 1 for completely correlated clutter up to the number of pulses M for completely uncorrelated clutter. Section 3.3.1 describes two definitions of L which have been used in the literature. Section 3.3.2 then presents the full derivation of the WTW detection method with implementation details in Section 3.3.3. The final Section 3.3.4 then shows how the WTW detection method can be supplemented with a different calculation method when the CNR is high.

3.3.1 Effective number of looks

The WTW detection method requires a way to relate the ACF to an 'effective number of looks'. There are two alternative methods which have been proposed in the literature. The first is by Barton [1969] who just considered the ratio of the correlation time to the observation time. Kanter [1986] derived the effective number of looks from this ratio in terms of the correlation value, $\tilde{\rho}$,

$$L' = \min\left[M, 1 - (M-1)\ln(\tilde{\rho})\right]. \tag{64}$$

where $0 \leq \tilde{\rho} \leq 1$ is a single parameter used to relate the de-correlation time model to a correlation value. This can be derived from a Gaussian ACF. Consider the discretised ACF for the nth pulse, where the sample rate is the PRF, f_{PRF}

$$\rho_n = \exp\left[-\frac{n^2}{f_{PRF}^2 T^2}\right] = \tilde{\rho}^{n^2}. \tag{65}$$

The second method is the ratio of the squared mean to the variance for correlated gamma random variables and relates to the ACF directly. The result was originally obtained by Kotz & Neumann [1963] and later derived independently by Kanter [1986]. If the values of the ACF are represented by ρ_n, the effective number of looks $L \leq M$ is given by

$$L = \frac{M^2}{M + 2\sum_{n=1}^{M-1}(M-n)|\rho_n|^2}. \tag{66}$$

This expression has a better statistical justification and is more general since all the correlation lags are used. For comparison, Figure 9 shows the number of effective looks for each case using the Gaussian ACF. Although both offer similar results, the second expression has a smoother response as the correlation increases.
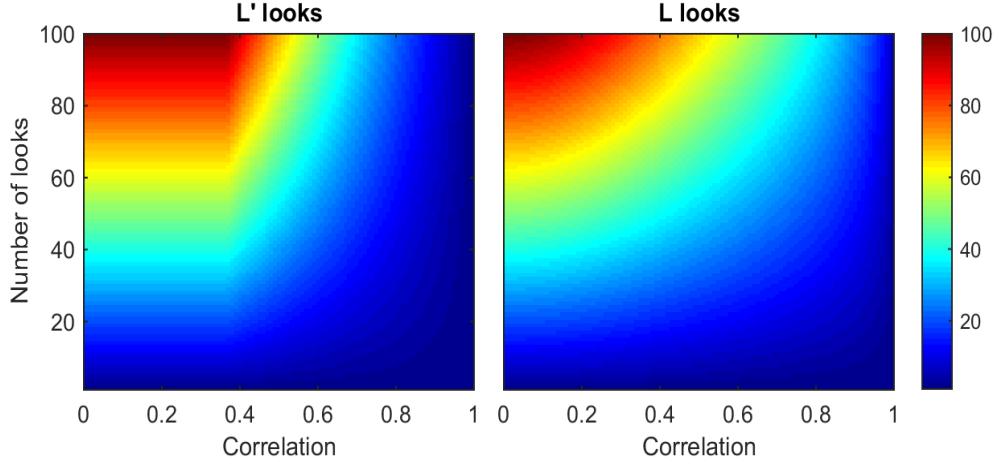
Figure 9: Effective number of looks comparison with varying correlation level and number of looks, M: left - L', right - L.

3.3.2 Ward, Tough and Watts calculation method

The WTW calculation method is described in [Ward, Tough & Watts 2013, Section 12.4] and provides a way of calculating the detection probability for both uncorrelated and correlated clutter with independent noise and target returns. The algorithm introduces the quantity β as the target plus clutter summed over L independent looks. If the SIR parameters s and S are now normalised by only the noise power p_n

$$\tilde{s} = \frac{1}{p_n} \sum_{m=1}^{M} A_m^2, \tag{67}$$

$$\tilde{S} = \frac{M \langle A^2 \rangle}{p_n} \tag{68}$$

and the speckle mean power, x is re-normalised according to

$$\alpha = \frac{Mx}{Lp_n} \tag{69}$$

then the probability density function of β is an L pulse Rice distribution [Ward, Tough & Watts 2013, Equation 12.33]

$$P(\beta|\tilde{s}, \alpha, L) = \frac{1}{\alpha} \left(\frac{\beta}{\tilde{s}} \right)^{(L-1)/2} \exp\left(-\frac{\tilde{s}+\beta}{\alpha} \right) I_{L-1}\left(\frac{2\sqrt{\tilde{s}\beta}}{\alpha} \right)$$

$$= \exp\left(-\frac{\tilde{s}+\beta}{\alpha} \right) \sum_{k=0}^{\infty} \frac{1}{k!\Gamma(L+k)} \tilde{s}^k \beta^{L-1+k} \alpha^{-L-2k} \tag{70}$$

where the Bessel function was expanded using Equation 50. With this normalisation, the target, clutter speckle and noise returns are given by

$$\tilde{\mu} = \frac{1}{p_n} \sum_{m=1}^{M} z_m \tag{71}$$

with the PDF given by [Ward, Tough & Watts 2013, Equation 12.36]:

$$
\begin{aligned}
P(\tilde{\mu}|\beta, M) &= \left(\frac{\tilde{\mu}}{\beta}\right)^{(M-1)/2} e^{-(\tilde{\mu}+\beta)} I_{M-1}\left(2\sqrt{\tilde{\mu}\beta}\right) \\
&= e^{-(\tilde{\mu}+\beta)} \left(\frac{\tilde{\mu}}{\beta}\right)^{(M-1)/2} \sum_{k=0}^{\infty} \frac{1}{k!\Gamma(M+k)} (\tilde{\mu}\beta)^{(M-1+2k)/2} \\
&= e^{-(\tilde{\mu}+\beta)} \sum_{k=0}^{\infty} \frac{1}{k!\Gamma(M+k)} \tilde{\mu}^{M-1+k}\beta^{k} \\
&= \sum_{k=0}^{\infty} \frac{e^{-\tilde{\mu}}\tilde{\mu}^{M+k-1}}{(M+k-1)!} \frac{e^{-\beta}\beta^{k}}{k!}.
\end{aligned}
\tag{72}
$$

Once the fluctuations due to β and $\tilde{s}$ are included, the PDF then becomes

$$
P(\tilde{\mu}|M, L, \alpha, \tilde{S}, K) = \int_0^{\infty}\int_0^{\infty} P(\tilde{\mu}|\beta, M)P(\beta|\tilde{s}, \alpha, L)P(\tilde{s}|\tilde{S}, K)d\beta d\tilde{s}
\tag{73}
$$

where the target fluctuation, $P(\tilde{s}|\tilde{S}, K)$ is given in Equation 56. The solution of this PDF for the cases of correlated clutter and noise and a target present in correlated clutter can be found in Appendix A. It is also not immediately obvious that this PDF is equivalent to the uncorrelated case when the effective number of looks L equals the number of pulses M. Appendix B presents a consistency check for a non-fluctuating target which verifies that these two PDFs are in fact equivalent.

Calculating of the probability of detection therefore requires the following integral to be evaluated

$$
\begin{aligned}
P_d(\tilde{\tau}|\beta, M) &= \int_{\tilde{\tau}}^{\infty} P(\tilde{\mu}|M, L, \alpha, \tilde{S}, K)d\tilde{\mu} \\
&= \sum_{k=0}^{M-1} e^{-\tilde{\tau}}\frac{\tilde{\tau}^{k}}{k!} + \sum_{k=M}^{\infty} e^{-\tilde{\tau}}\frac{\tilde{\tau}^{k}}{k!}\left(1 - \sum_{m=0}^{k-M}\left\langle\frac{e^{-\beta}\beta^{m}}{m!}\right\rangle\right)
\end{aligned}
\tag{74}
$$

where the threshold, $\tilde{\tau}$ is now normalised by only the noise power and does not depend on the mean clutter power x.

$$
\tilde{\tau} = Y/p_n.
\tag{75}
$$

For the general fluctuating target case, the expectation in Equation 74 can be expanded as [Ward, Tough & Watts 2013, Equation 12.38 and 12.39]

$$
\begin{aligned}
\left\langle e^{-\beta}\frac{\beta^{m}}{m!}\right\rangle &= \int_0^{\infty}\int_0^{\infty} e^{-\beta}\frac{\beta^{m}}{m!}P(\beta|\tilde{s}, \alpha, L)P(\tilde{s}|\tilde{S}, K)d\tilde{s}d\beta \\
&= \int_0^{\infty} \exp\left(-\beta\frac{\alpha+1}{\alpha}\right)\left(\frac{K}{\tilde{S}}\right)^K \sum_{k=0}^{\infty} \frac{(k+K-1)!}{m!k!\Gamma(L+k)\Gamma(K)}\left(\frac{\alpha\tilde{S}}{\tilde{S}+\alpha K}\right)^{k+K} \\
&\quad \times \beta^{L+m+k-1}\alpha^{-L-2k}d\beta
\end{aligned}
\tag{76}
$$

where the definite integral [Gradshteyn & Ryzhik 1994, §3.351/3] has been used:

$$
\int_0^{\infty} x^m e^{-ax}dx = m!a^{-m-1}.
\tag{77}
$$

The second integral can then be evaluated as

$$
\left\langle e^{-\beta} \frac{\beta^m}{m!} \right\rangle = \left(\frac{K}{\tilde{S}} \right) \sum_{k=0}^{\infty} \frac{(k+K-1)!(L+m+k-1)!}{m!k!\Gamma(L+k)\Gamma(K)} \left(\frac{\alpha\tilde{S}}{\tilde{S}+\alpha K} \right)^{k+K} \left(\frac{\alpha}{\alpha+1} \right)^{L+m+k} \alpha^{-L-2k}
$$

$$
= \frac{\alpha^m}{m!(\alpha+1)^{L+m}} \left(\frac{\alpha K}{\tilde{S}+\alpha K} \right)^K \sum_{k=0}^{\infty} \frac{(k+K-1)!(L+m+k-1)!}{k!\Gamma(L+k)\Gamma(K)} \left(\frac{\tilde{S}}{(\tilde{S}+\alpha K)(\alpha+1)} \right)^k
$$

$$
= \frac{(L+m-1)!}{m!(L-1)!} \frac{\alpha^m}{(\alpha+1)^{L+m}} \left(\frac{\alpha K}{\tilde{S}+\alpha K} \right)^K
$$

$$
\times \sum_{k=0}^{\infty} \frac{\Gamma(k+K)\Gamma(L+m+k)\Gamma(L)}{k!\Gamma(L+k)\Gamma(K)\Gamma(L+m)} \left(\frac{\tilde{S}}{(\tilde{S}+\alpha K)(\alpha+1)} \right)^k
$$

$$
= \frac{(L+m-1)!}{m!(L-1)!} \frac{\alpha^m}{(\alpha+1)^{L+m}} \left(\frac{\alpha K}{\tilde{S}+\alpha K} \right)^K {}_2F_1\left(K, L+m; L; \frac{\tilde{S}}{(\tilde{S}+\alpha K)(\alpha+1)} \right) \quad (78)
$$

where the hypergeometric function ${}_2F_1$ is obtained from [Gradshteyn & Ryzhik 1994, §9.14 and §9.131/1]:

$$
{}_2F_1(K, L+m, L, \eta) = \sum_{k=0}^{\infty} \frac{\Gamma(K+k)\Gamma(L+m+k)\Gamma(L)}{k!\Gamma(K)\Gamma(L+m)\Gamma(L+k)} \eta^k
$$

$$
= \sum_{k=0}^{\infty} \frac{(K)_k(L+m)_k}{k!(L)_k} \eta^k
$$

$$
= \frac{1}{(1-\eta)^K} {}_2F_1\left(K, -m, L, \frac{\eta}{\eta-1} \right) \quad (79)
$$

with $\eta = \dfrac{\tilde{S}}{(\tilde{S}+\alpha K)(\alpha+1)}$ and $(\cdot)_k$ is the Pochhammer symbol, $(x)_k = \Gamma(x+k)/\Gamma(x)$. With this manipulation, Equation 78 can be written as

$$
\left\langle e^{-\beta} \frac{\beta^m}{m!} \right\rangle = \frac{(L+m-1)!}{m!(L-1)!} \frac{\alpha^m}{(\alpha+1)^{L+m}} \left(\frac{K(\alpha+1)}{\tilde{S}+K(\alpha+1)} \right)^K {}_2F_1\left(K, -m; L; \frac{-\tilde{S}}{\alpha(\tilde{S}+K(\alpha+1))} \right).
$$
$$
\quad (80)
$$

If the recurrence relation for the hypergeometric function [Gradshteyn & Ryzhik 1994, §9.137/3] is compared with the recurrence relation for the function Ψ [Ward, Tough & Watts 2013, Equation 12.40], it can be established that $\Psi(m, L, K, z) = {}_2F_1(K, -m, L, -z)$.

For the constant target case, $P(\beta|\tilde{S}, \alpha, L)$ is obtained from Equation 70 with $\tilde{s} = \tilde{S}$ and the

expectation in Equation 74 becomes

$$
\begin{aligned}
\left\langle e^{-\beta}\frac{\beta^m}{m!}\right\rangle &= \int_0^\infty e^{-\beta}\frac{\beta^m}{m!}P(\beta|\tilde{S},\alpha,L)d\beta \\
&= \int_0^\infty \exp\left(-\beta\frac{\alpha+1}{\alpha}\right)\sum_{k=0}^\infty \frac{\tilde{S}^k e^{-\tilde{S}/\alpha}}{m!k!\Gamma(L+k)}\beta^{L+m+k-1}\alpha^{-L-2k}d\beta \\
&= \sum_{k=0}^\infty \frac{(L+m+k-1)!}{m!k!\Gamma(L+k)}\tilde{S}^k e^{-\tilde{S}/\alpha}\left(\frac{\alpha}{\alpha+1}\right)^{L+m+k}\alpha^{-L-2k} \\
&= \frac{(L+m-1)!}{m!(L-1)!}\frac{\alpha^m}{(\alpha+1)^{L+m}}e^{-\tilde{S}/\alpha}\sum_{k=0}^\infty \frac{\Gamma(L)\Gamma(L+m+k)}{k!\Gamma(L+k)\Gamma(L+m)}\left(\frac{\tilde{S}}{\alpha(\alpha+1)}\right)^k \\
&= \frac{(L+m-1)!}{m!(L-1)!}\frac{\alpha^m}{(\alpha+1)^{L+m}}e^{-\tilde{S}/\alpha}\sum_{k=0}^\infty \frac{(L+m)_k}{k!(L)_k}\left(\frac{\tilde{S}}{\alpha(\alpha+1)}\right)^k \\
&= \frac{(L+m-1)!}{m!(L-1)!}\frac{\alpha^m}{(\alpha+1)^{L+m}}e^{-\tilde{S}/\alpha}{}_1F_1\left(L+m,L;\frac{\tilde{S}}{\alpha(\alpha+1)}\right) \\
&= \frac{(L+m-1)!}{m!(L-1)!}\frac{\alpha^m}{(\alpha+1)^{L+m}}e^{-\tilde{S}/(\alpha+1)}{}_1F_1\left(-m,L;-\frac{\tilde{S}}{\alpha(\alpha+1)}\right) \quad (81)
\end{aligned}
$$

where ${}_1F_1$ is the confluent hypergeometric function and the relationship [Gradshteyn & Ryzhik 1994, §9.212/1] has been used:

$$
{}_1F_1(\alpha,\gamma;z) = e^z {}_1F_1(\gamma-\alpha,\gamma;-z). \quad (82)
$$

If the recurrence relation for the function Φ [Ward, Tough & Watts 2013, Equation 12.42] is compared with the recurrence relation for the confluent hypergeometric function [Gradshteyn & Ryzhik 1994, §9.212/4], it can be established that $\Phi(m,L,z) = {}_1F_1(-m,L;-z)$.

This result can also be expressed in terms of a Laguerre polynomial by using the relationship [Gradshteyn & Ryzhik 1994, §8.972/1]:

$$
\mathcal{L}_m^n(x) = \left(\begin{array}{c} m+n \\ m \end{array}\right){}_1F_1(-m,n+1;x). \quad (83)
$$

With this relationship, Equation 81 can be written as

$$
\left\langle e^{-\beta}\frac{\beta^m}{m!}\right\rangle = \frac{\alpha^m}{(\alpha+1)^{L+m}}e^{-\tilde{S}/(\alpha+1)}\mathcal{L}_m^{L-1}\left(-\frac{\tilde{S}}{\alpha(\alpha+1)}\right). \quad (84)
$$

Then the identity [Gradshteyn & Ryzhik 1994, §8.975/1]

$$
\sum_{m=0}^\infty \mathcal{L}_m^n(x)z^m = (1-z)^{-n-1}\exp\left(\frac{xz}{z-1}\right) \quad (85)
$$

can be used to verify that

$$
\sum_{m=0}^\infty \left\langle \frac{e^{-\beta}\beta^m}{m!}\right\rangle = 1. \quad (86)
$$

3.3.3 Evaluating the detection probability

Before evaluating the detection probability, Chernoff bounds [Shnidman 1976, Wozencraft & Jacobs 1965] are first calculated to check whether the result can be approximated as either 0 or 1. Otherwise, the detection probability in Equation 74 can be evaluated by re-writing it as the sum of the product of two series, A_m and C_m:

$$P_d(\tilde{\tau}|\beta, M) = \sum_{m=m_0}^{m_1} A_m C_m \tag{87}$$

where m_0 and m_1 are the lower and upper summation limits. Details of both the Chernoff bounds and the upper and lower limits are given in Appendix C. The first series in the sum is given by

$$\begin{aligned} A_{m_0} &= \exp\left(m_0 \ln \tilde{\tau} - \tilde{\tau} - \ln \Gamma(m_0 + 1)\right), \\ A_{m+1} &= \tilde{\tau} A_m/(m+1) \end{aligned} \tag{88}$$

and does not need to be recalculated for different values of x since the threshold $\tilde{\tau}$ is independent of the clutter power x. The second series is

$$C_m = \begin{cases} 1, & m < M \\ 1 - \displaystyle\sum_{k=0}^{m-M} B_k, & m \geq M \end{cases} \tag{89}$$

where B_k denotes the expectation

$$B_k = \left\langle \frac{e^{-\beta} \beta^k}{k!} \right\rangle. \tag{90}$$

The coefficients for the two target cases in Equations 80 and 81 can be evaluated using recurrence relations [Ward, Tough & Watts 2013]. For the fluctuating target in Equation 80,

$$\begin{aligned} B_0 &= \frac{1}{(\alpha+1)^L} \left(\frac{K(\alpha+1)}{\tilde{S} + K(\alpha+1)}\right)^K, \\ B_1 &= L\frac{\alpha}{\alpha+1}\left(1 + \frac{K\tilde{z}}{L}\right)B_0, \\ B_{k+1} &= \frac{1}{k+1}\frac{\alpha}{\alpha+1}\left((L + 2k + (k+K)\tilde{z})B_k - (L-1+k)(\tilde{z}+1)\left(\frac{\alpha}{\alpha+1}\right)B_{k-1}\right) \end{aligned} \tag{91}$$

where $\tilde{z} = \dfrac{\tilde{S}}{\alpha\left(\tilde{S} + K(\alpha+1)\right)}$. For the constant target case in Equation 81,

$$\begin{aligned} B_0 &= \frac{1}{(\alpha+1)^L}\exp\left(-\frac{\tilde{S}}{\alpha+1}\right), \\ B_1 &= L\frac{\alpha}{\alpha+1}\left(1 + \frac{\tilde{Z}}{L}\right)B_0, \\ B_{k+1} &= \frac{1}{k+1}\frac{\alpha}{\alpha+1}\left(\left(L + 2k + \tilde{Z}\right)B_k - (L-1+k)\left(\frac{\alpha}{\alpha+1}\right)B_{k-1}\right) \end{aligned} \tag{92}$$

where $\tilde{Z} = \dfrac{\tilde{S}}{\alpha(\alpha+1)}$. Even with high precision arithmetic, the series in Equations 91 and 92 are prone to underflow for large $\tilde{S}/\alpha$. To avoid this, a method suggested in Section IV-A of [Shnidman 1995] is used. First $\ln(B_0)$ is calculated separately and stored in a variable v_0. The series is started at 1 and each term is checked to see if it exceeds e^{25}. If it does, all terms are divided by e^{25} and 25 is added to v_0. Once all required terms have been computed, the sum of the series is multiplied by $\exp(v_0)$. In the constant target case the recurrence for B_k is the g-function, and in the fluctuating target case the h-function, both defined by Shnidman [1995]. However the application of these functions is different here. The clutter model of [Shnidman 1995] is compared with the compound K distribution in [Shnidman 2005].

Note that this calculation method can also be used to calculate the P_{fa} by setting $\tilde{S} = 0$ and using the coefficients:

$$
\begin{aligned}
B_0 &= \frac{1}{(\alpha+1)^L}, \\
B_{k+1} &= \frac{L+k}{k+1}\frac{\alpha}{\alpha+1}B_k.
\end{aligned}
\tag{93}
$$

3.3.4   Detection at high CNR

As the CNR increases, the method of Ward, Tough & Watts [2013] becomes computationally intensive and fails completely when there is only clutter present. The method of [Shnidman 1976, Shnidman 1989, Shnidman 1991] can be used if it is modified for a real effective number of looks $L \geq 1$ in place of an integer number M. Consider a constant target where the target plus interference PDF is described by Equation 49. The probability of detection is then given by

$$
\begin{aligned}
P_d(\tau|x,L) &= \int_\tau^\infty P(\mu|s,L)d\mu \\
&= \sum_{k=0}^\infty \frac{e^{-s}s^k}{k!}\frac{1}{\Gamma(L+k)}\int_\tau^\infty e^{-\mu}\mu^{L+k-1}d\mu \\
&= \sum_{k=0}^\infty \frac{e^{-s}s^k}{k!}\frac{\Gamma(L+k,\tau)}{\Gamma(L+k)}.
\end{aligned}
\tag{94}
$$

If $L = l + \delta$, where $l = \text{floor}(L)$, then using an identity for the incomplete gamma function [Gradshteyn & Ryzhik 1994, §8.356/5]:

$$
P_d(\tau|x,l,\delta) = \sum_{k=0}^\infty \frac{e^{-s}s^k}{k!}\left(\frac{\Gamma(\delta+1,\tau)}{\Gamma(\delta+1)} + \sum_{n=0}^{l+k-2}\frac{e^{-\tau}\tau^{\delta+n+1}}{\Gamma(\delta+n+2)}\right).
\tag{95}
$$

Then by making the substitution $m = \delta + n + 1$, where the index m is a real number, gives

$$
\begin{aligned}
P_d(\tau|x,L,\delta) &= \sum_{k=0}^{\infty} \frac{e^{-s}s^k}{k!} \left(\frac{\Gamma(\delta+1,\tau)}{\Gamma(\delta+1)} + \sum_{m=\delta+1}^{L+k-1} \frac{e^{-\tau}\tau^m}{\Gamma(m+1)} \right) \\
&= \sum_{k=0}^{\infty} \frac{e^{-s}s^k}{k!} \left(\frac{\Gamma(\delta+1,\tau)}{\Gamma(\delta+1)} + \sum_{m=\delta+1}^{L-1} \frac{e^{-\tau}\tau^m}{\Gamma(m+1)} + \sum_{m=L}^{L+k-1} \frac{e^{-\tau}\tau^m}{\Gamma(m+1)} \right) \\
&= \frac{\Gamma(\delta+1,\tau)}{\Gamma(\delta+1)} + \sum_{m=\delta+1}^{L-1} \frac{e^{-\tau}\tau^m}{\Gamma(m+1)} + \sum_{k=0}^{\infty} \frac{e^{-s}s^k}{k!} \sum_{m=L}^{L+k-1} \frac{e^{-\tau}\tau^m}{\Gamma(m+1)} \\
&= \frac{\Gamma(\delta+1,\tau)}{\Gamma(\delta+1)} + \sum_{m=\delta+1}^{L-1} \frac{e^{-\tau}\tau^m}{\Gamma(m+1)} + \sum_{k=0}^{\infty} \frac{e^{-\tau}\tau^m}{\Gamma(m+1)} \left(1 - \sum_{k=0}^{m-L} \frac{e^{-s}s^k}{k!} \right).
\end{aligned} \quad (96)
$$

This expression differs from the original summation in Equation 52 in two respects: the first term is new and the index m is a real number rather than an integer, beginning at $m = \delta + 1$ and incremented by 1 for each successive term in the sum. When L is an integer, $\delta = 0$ and the first term is just $e^{-\tau}$ as in the original series. For large τ the original sum must be started at some term $n_0 > 0$ to avoid underflow and loss of significance (see Appendix C.2 for details). In this case the first term in Equation 96 is negligible and the sum is started at $m_0 = n_0 + \delta$.

The same modification can easily be applied to the series in Equation 58 for a fluctuating target. Note that the target fluctuation parameter K is the same as for detection in uncorrelated clutter, so for example $K = M$ for a Swerling 2 target in both cases. Figure 10 shows the effect of varying the clutter to noise ratio on the probability of detection for a Swerling 2 target in exponentially distributed clutter with $M = 10$ and $L = 1.5$. The dashed black line is calculated using the method described here for clutter only (infinite CNR) and the other curves are calculated with the method of Ward, Tough and Watts.

To determine the optimal CNR for switching between methods, the maximum SIR error between the WTW and the modified Shnidman method has been measured. As described in the following section, both of these calculation methods can be extended to compound distributions. The Pareto distribution has been used to model the clutter with a shape of 3 and the number of looks, $M = 5$. To establish the worst error, the speckle is totally correlated with $\tilde{\rho} = 1$ and hence $L = 1$. Fig. 11 shows the maximum SIR error and the mean run time averaged over 3 runs as a function of the CNR. As expected, the SIR error is 0.7 dB when the CNR is at -10 dB due to the incorrect modelling of the correlated thermal noise. However, this quickly reduces and becomes less than 0.1 dB at 0 dB. While the WTW detection method is more accurate, it is far more computationally intensive. At the same transition point when the CNR is 0 dB, the run time is around 10 s and increases to 70 s at 10 dB. For comparison, the mean run time for the modified Shnidman algorithm with any value of CNR is 0.14 s. From this result, a realistic transition point between algorithms would be at 0 dB or when the clutter starts to dominate the interference.
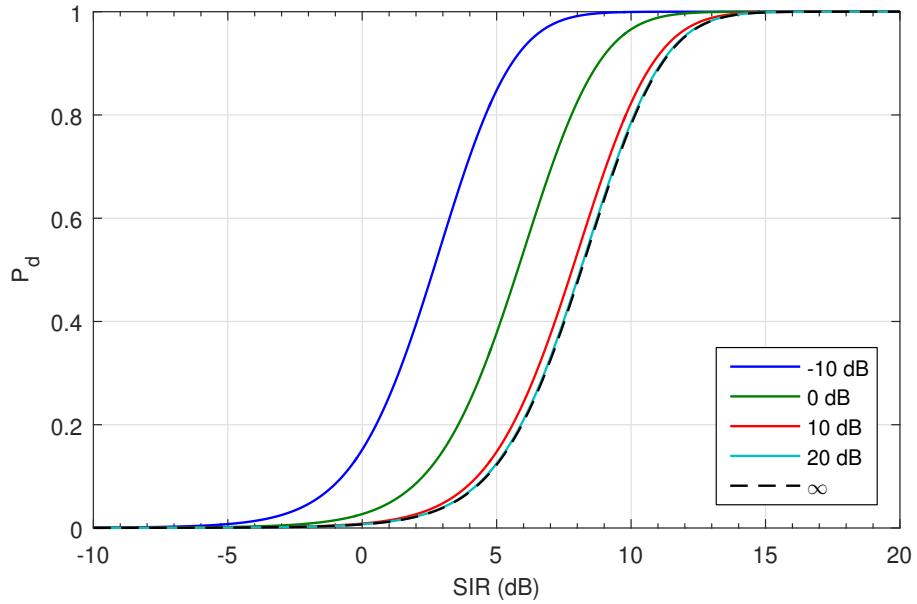
Figure 10: P_d with different clutter to noise ratios for a Swerling 2 target in exponentially distributed clutter and noise after non-coherent integration of 10 pulses with a P_{fa} of 10^{-4}. The effective number of independent clutter samples is 1.5.
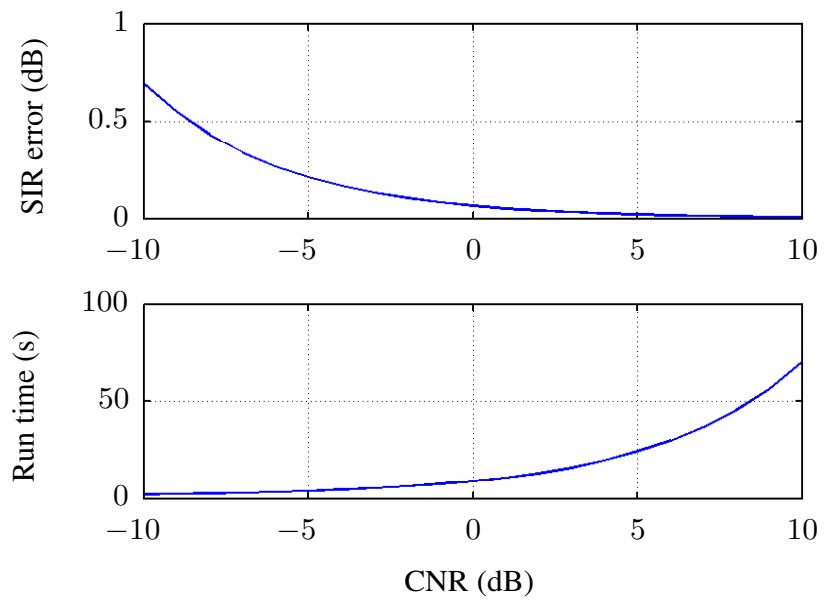

Figure 11: Maximum SIR error between detection algorithms (top) and mean run time for WTW algorithm (bottom).

3.4 Detection in compound clutter

Thus far the clutter power x has been treated as a constant. In the compound model x is a random variable with a PDF $P_x(x)$. The global probability of detection P'_d is obtained by integrating the local P_d over this PDF. The effect of this 'smoothing' is to degrade the non-coherent integration by up to 20 dB when compared to homogeneous Gaussian clutter [Allen & Urkowitz 1993].

With this extension, the local SIR, S is now replaced by a global SIR, S' and the local threshold. τ by a global threshold, τ',

$$S' = \frac{M \langle A^2 \rangle}{p_c + p_n}, \tag{97}$$

$$\tau' = \frac{Y}{p_c + p_n} \tag{98}$$

These can both be rewritten in terms of the short scale definitions,

$$S = \frac{S'(p_c + p_n)}{x + p_n}, \tag{99}$$

$$\tau = \frac{\tau'(p_c + p_n)}{x + p_n}. \tag{100}$$

The P_d solution is determined by multiplying the PDF of the mean speckle power, $P_x(x)$ and then integrating over x,

$$P'_{d,K}(\tau'|S', M) = \int_0^\infty P_x(x) P_{d,K} \left(\frac{\tau'(p_c + p_n)}{x + p_n} | \frac{S'(p_c + p_n)}{x + p_n}, M \right) dx. \tag{101}$$

To the authors' knowledge, there is no documented analytic solution to this integral and numerical integration must be used for evaluation as described in Section 2.3 of [Bocquet 2012]. Different target fluctuations can be modelled by changing the value of K as in the previous section. The solution for P'_d can be expressed in terms of τ', S' and the CNR, C'. If the integration variable is redefined as $u = x/p_c$,

$$\begin{aligned} P'_{d,K}(\tau'|S', M, C') &= \int_0^\infty \frac{1}{p_c} P_x \left(\frac{x}{p_c} \right) P_{d,K} \left(\frac{\tau'(C'+1)}{x/p_c C'+1} | \frac{S'(C'+1)}{x/p_c C'+1}, M \right) dx \\ &= \int_0^\infty P_u(u) P_{d,K} \left(\frac{\tau'(C'+1)}{uC'+1} | \frac{S'(C'+1)}{uC'+1}, M \right) du \end{aligned} \tag{102}$$

where $P_x(u) = 1/p_c P_x(x/p_c)$ and $dx = p_c du$.

The probability of false alarm can be calculated similarly,

$$P'_{fa,K}(\tau'|M, C') = \frac{1}{\Gamma(M)} \int_0^\infty P_u(u) \Gamma \left(M, \frac{\tau'(C'+1)}{uC'+1} \right) du \tag{103}$$

where again numerical integration can be used for evaluation.

For the WTW method, the same procedure is applied, except that the parameters $\tilde{S}$ and $\tilde{\tau}$ are normalised by the noise power alone and hence are independent of x. If these parameters are

renormalised by the sum of clutter and noise powers we obtain

$$\tilde{S}' = \frac{\tilde{S}}{C' + 1}, \tag{104}$$

$$\tilde{\tau}' = \frac{\tilde{\tau}}{C' + 1}. \tag{105}$$

The dependence on x is only through the parameter α,

$$\alpha = \frac{Mx}{Lp_n} = \frac{M}{L} u C'. \tag{106}$$

4 Detection performance analysis

This section presents target detection performance results using the empirical models from Section 2. In these results, the Pareto distribution acts as a proxy for the data as it has been shown to match extremely well, [Rosenberg & Bocquet 2013a]. By accounting for temporal correlation and comparing the differences in detection performance between the K and Pareto distributions, this analysis also highlights the importance of using the correct model when assessing detection performance. The outcome of this section is an accurate description of the detection performance given a variety of target fluctuation models, collection geometries and environmental conditions.

As a basis for the modelling results, a common set of radar parameters are described in Table 6. The modelled outputs described in Section 2.3.2 are then shown in Tables 7-9 for a variety of geometries, polarisations and sea-states. The trends for the shape parameters include a linear increase with grazing angle, an increase with sea-state and a maximum in the upwind direction. Also, due to the effect of the platform motion, the overall decorrelation time, T', from Equation 29 is typically smaller than the temporal decorrelation, T, from Equation 30. The clutter correlation is determined using the overall decorrelation time with the Gaussian model in Equation 65 and the effective number of looks is determined with Equation 66.

The first section 4.1 shows the false alarm rate for the K and Pareto distributions. Section 4.2 then describes the P_d results for a selection of fluctuating target models, false alarm rates, geometry and sea-states. This then leads into the final Section 4.3 which looks at the minimum detectable target RCS.

Table 6: Common simulation input parameters

Parameters	Symbol	Value
Centre frequency	f_c	10 GHz
Bandwidth	B	200 MHz
Pulse width	T_p	5 μs
PRF	f_{PRF}	500 Hz
Peak transmitted power	P_t	20 kW
Antenna gain (one way)	G	35 dB
Combined losses	$L_a + L_s$	7 dB
Noise figure	F_n	4 dB
Reference temperature	T_0	290 K
Azimuth beam width two-way 3 dB	ϕ_{3dB}	1°
Doppler spectrum mean	f_0	0 Hz
Platform velocity	v_p	100 m/s
Slant range	R	20 km
Elevation / grazing angle	θ	30°
Azimuth angle	ϕ	0°
Wind swell angle	ψ	0°
Sea-state	S	3
Number of looks	M	10
Probability of false alarm	P_{fa}	10^{-5}
Probability of detection	P_d	0.5
Polarisation		HH
Target fluctuation model		Swerling case 2

Table 7: *Calculated model parameters for varying azimuth angle with 30° grazing, sea-state 3.*

Polarisation	Azimuth angle	CNR (dB)	ν	a	T (ms)	T' (ms)
HH	Upwind	14.60	2.62	4.10		
	Crosswind	9.23	1.51	2.86	10.11	4.66
	Downwind	10.68	3.29	4.53		
HV	Upwind	3.22	7.18	8.15		
	Crosswind	0.63	1.36	2.53	11.43	4.78
	Downwind	2.68	5.62	7.91		
VV	Upwind	20.92	31.77	34.94		
	Crosswind	15.73	16.52	16.55	12.75	4.86
	Downwind	19.79	36.07	37.12		

Table 8: *Calculated model parameters for varying grazing angle with sea-state 3, upwind direction.*

Polarisation	Grazing angle	CNR (dB)	ν	a	T (ms)	T' (ms)
HH	20°	10.16	0.60	2.37		4.37
	30°	14.60	2.62	4.10	10.11	4.66
	45°	21.61	11.40	14.05		5.43
HV	20°	1.27	3.24	4.20		4.46
	30°	3.32	7.18	8.15	11.43	4.78
	45°	6.74	15.88	19.20		5.61
VV	20°	18.40	30.60	33.70		4.53
	30°	20.92	31.77	34.94	12.75	4.86
	45°	25.05	32.99	36.23		5.75

Table 9: *Calculated model parameters for varying sea state with 30° grazing, upwind direction.*

Polarisation	Sea state	CNR (dB)	ν	a	T (ms)	T' (ms)
HH	1	5.96	0.42	2.37	14.22	4.98
	3	14.6	2.62	4.10	10.11	4.66
	6	20.1	4.13	5.15	3.65	3.00
HV	1	−6.40	0.37	3.05	14.94	4.96
	3	3.32	7.18	8.15	11.43	4.78
	6	9.45	10.82	10.25	5.74	3.88
VV	1	11.32	22.07	23.06	15.63	4.98
	3	20.92	31.77	34.94	12.75	4.86
	6	26.98	29.92	32.17	7.83	4.36

4.1 Probability of false alarm

The probability of false alarm is related to the CCDF as shown in Equation 39. In a detection scheme, the desired P_{fa} is specified and the threshold must be found by inverting this equation. Using the parameters above, Figure 12 shows a comparison of P_{fa} for the K and Pareto distributions. A range of looks, M (non-coherent sum of pulses) has also been shown to demonstrate the effect of correlation.

There is a clearly a big difference in the HH and HV results with the K-distribution having a lower threshold by approximately 5 dB and 2 dB respectively at 10^{-5}, while there is only a minor difference in the VV channel. The effect of non-coherently integrating pulses is to reduce the threshold. This effect is more pronounced in the VV polarisation where the threshold is reduced by 6 dB with 50 pulses integrated.
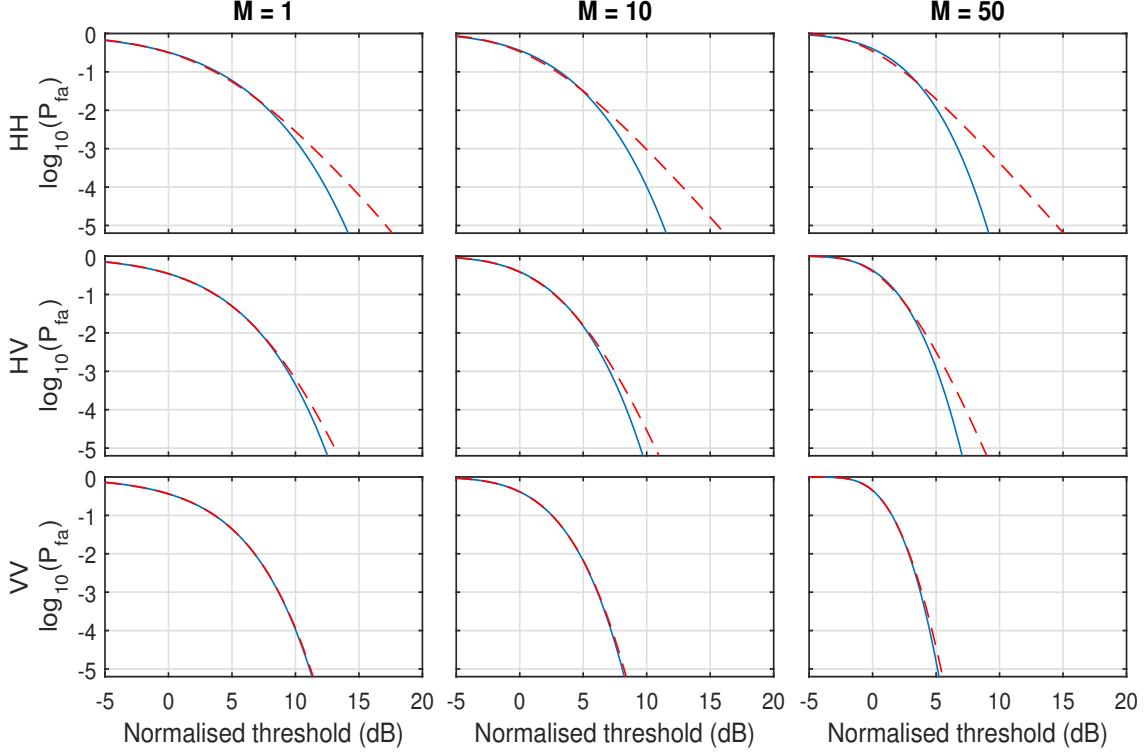

Figure 12: P_{fa} comparison with number of looks: (—) K, (- -) Pareto.

4.2 Probability of detection

Once a P_{fa} is chosen and the threshold is found, the detection probability, P_d can be calculated as a function of the Signal to Interference Ratio (SIR). The next set of results in Figures 13-17 show variations in the target model, number of looks, geometry and sea-state.

The target fluctuation models can all be derived from the chi-squared distribution model in Equation 56. A non-fluctuating Marcum target model is found when $K \to \infty$. Using the Pareto distribution, the P_d result is shown along the top row of Figure 13 for $M = 1, 10$ and 50 looks and a P_{fa} of 10^{-5}. As the number of looks increases, the curve shifts to the left and the required SIR for a contant P_d is reduced. The Swerling fluctuation models 1 and 2 refer to the cases where $K = 1$ and $K = M$ and the target model becomes an exponential distribution. Similarly, the Swerling models 3 and 4 refer to a chi-squared distribution with $K = 2$ and $K = 2M$. To account for target correlation, an effective value $B \le M$ can be determined using the relationship in Equation 66 with an appropriate target ACF. For targets with an exponential distribution, the fluctuation parameter is related by $K = B$, while for chi-squared distributions, the relationship is $K = 2B$. If a Gaussian ACF is assumed for the target as in Equation 65, then the detection

performance can be calculated as a function of the target correlation, $\rho_t(n) = \tilde{\rho}_t^{n^2}$ for $n = 0, \ldots, M-1$. For $\tilde{\rho}_t = 0$, the target is uncorrelated and $B = 1$, while $\tilde{\rho}_t = 1$ implies total correlation and $B = M$. Figure 13 shows a comparison for both exponential and chi-squared target models as the number of looks increases. The increasing number of looks has again shifted the curves to the left, while an increasing target correlation reduces the slope of the curve. In all cases, the chi-squared result has a slightly steeper slope than the exponential fluctuation. Since the target correlation cannot be known in advance, only the uncorrelated exponential fluctuation (Swerling 2) model is used for the remainder of these comparisons. Table 10 shows the minimum required SIR for a $P_d = 0.5$.

Using a model also allows us to extrapolate down to lower P_{fa} levels than could be used in a real detection scheme. The result in Figure 14 shows the K and Pareto distribution results for a P_{fa} of 10^{-4}, 10^{-5} and 10^{-6}. For both the HH and HV polarisations, there is a clear difference between the two distribution models which increases as the P_{fa} reduces. For the HH polarisation, the difference in the SIR at a P_d of 0.5 is up to 5.4 dB, while this difference is reduced for the cross-pol polarisation and almost zero for VV. Table 11 shows the required SIR for each result measured at a P_d of 0.5.

The next three results show a comparison with geometry and sea-state. Figure 15 first shows the variation in azimuth direction. The biggest variation between the K and Pareto distributions is found for HH and HV crosswind directions where the SIR difference is up to 7.4 dB. There is little difference in the VV polarisation, where the Pareto matches the K distribution result. Table 12 shows the required SIR for each result measured at a P_d of 0.5.

Figure 16 shows a comparison of $20°$, $30°$ and $45°$ grazing. The biggest difference between the distributions is found in the HH polarisation where the SIR difference is up to 5.1 dB for $20°$ grazing. The mismatch is reduced for the VV polarisation and also when the grazing angle gets higher. Table 13 shows the required SIR for each result measured at a P_d of 0.5.

The final result in Figure 17 shows the variation in sea-state. The largest mismatch of 5.1 dB is found for the lowest sea-state in the HH polarisation. The mismatch reduces as the sea-state increases and is very small for the VV polarisation. For the lowest sea-state, the CNR for the HV channel is very low and both distributions are approximately exponential giving the same performance results. Table 14 shows the required SIR for each result measured at a P_d of 0.5.

Table 10: Required SIR (dB) at a P_d of 0.5. Variation in target model and number of looks corresponding to Figure 13.

| M	1	10	50
Marcum	16.66	14.54	13.50
Exponential, $\rho_t = 1$ (Swerling 1)	18.23	16.11	15.07
Exponential, $\rho_t = 0$ (Swerling 2)	18.23	14.67	13.51
Chi-squared, $\rho_t = 1$ (Swerling 3)	17.40	15.28	14.24
Chi-squared, $\rho_t = 0$ (Swerling 4)	17.40	14.60	13.50
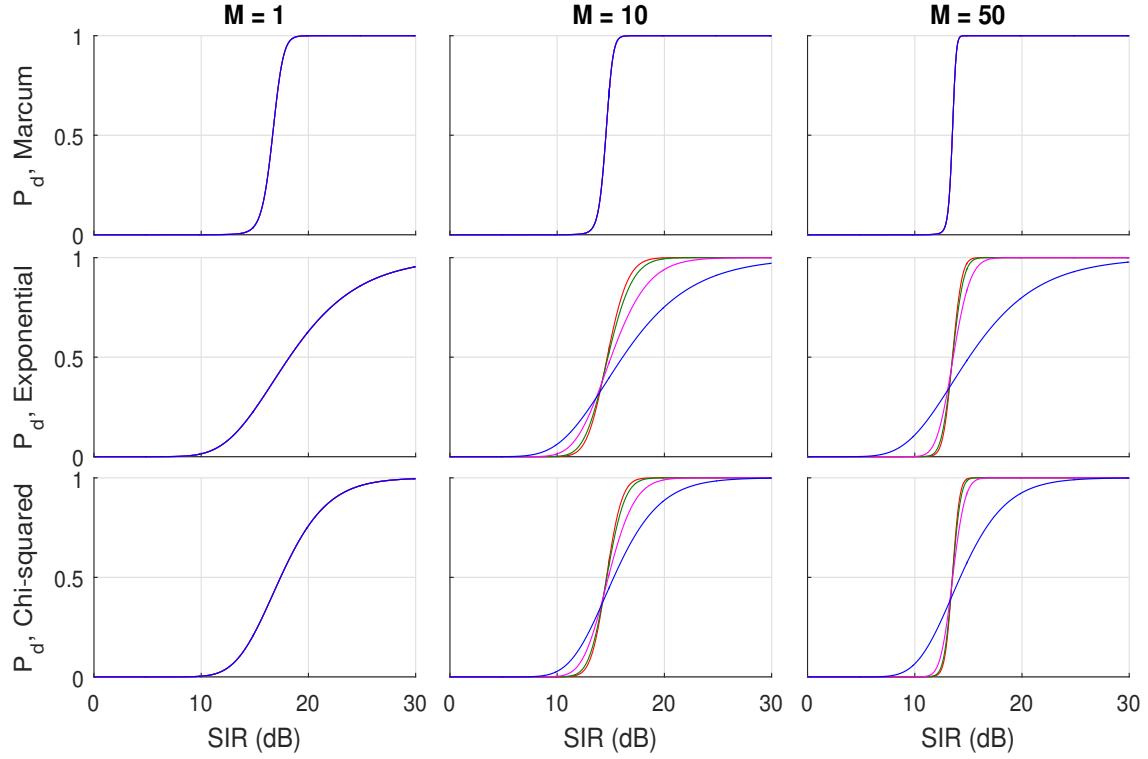
DST-Group–TR–3193

Figure 13: P_d variation with target model and number of looks. Variation with target correlation: $\tilde{\rho}_t$: (—) 0, (—) 0.5, (—) 0.9, (—) 1.
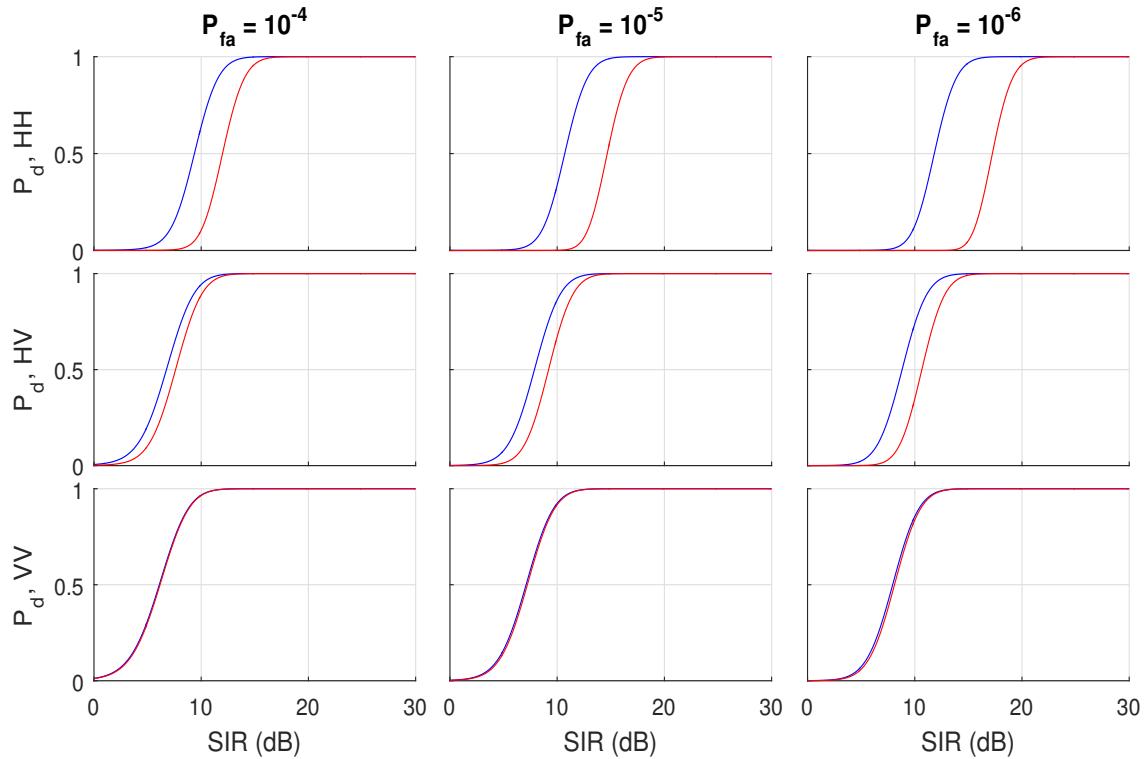

Figure 14: P_d variation with polarisation and false alarm rate: (—) K, (—) Pareto.

DST-Group–TR–3193

Table 11: Required SIR (dB) at a P_d of 0.5. Variation in false alarm rate corresponding to Figure 14.

Pol.	$P_{\text{fa}} = 10^{-4}$		$P_{\text{fa}} = 10^{-5}$		$P_{\text{fa}} = 10^{-6}$	
	K	Pareto	K	Pareto	K	Pareto
HH	9.37	11.99	10.71	14.67	11.82	17.24
HV	6.76	7.61	7.88	9.20	8.82	10.66
VV	6.10	6.16	7.10	7.22	7.94	8.11

Table 12: Required SIR (dB) at a P_d of 0.5. Variation in azimuth angle corresponding to Figure 15.

| Pol.	Upwind, $\phi = 0°$		Crosswind, $\phi = 90°$		Downwind, $\phi = 180°$	
	K	Pareto	K	Pareto	K	Pareto
HH	10.71	14.67	11.80	18.16	10.03	13.65
HV	7.88	9.20	10.28	17.63	8.11	9.15
VV	7.10	7.22	7.66	8.28	7.01	7.16
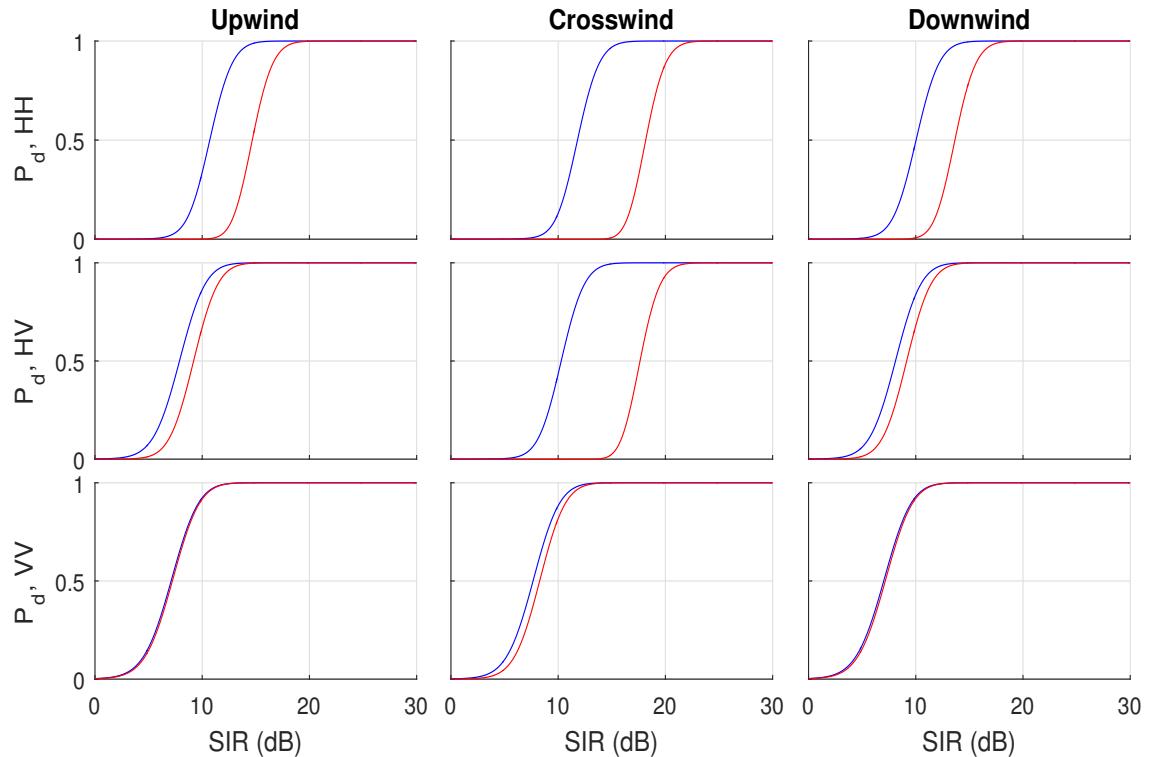
*Figure 15: P_d variation with polarisation and azimuth angle: (—) K, (—) Pareto.*
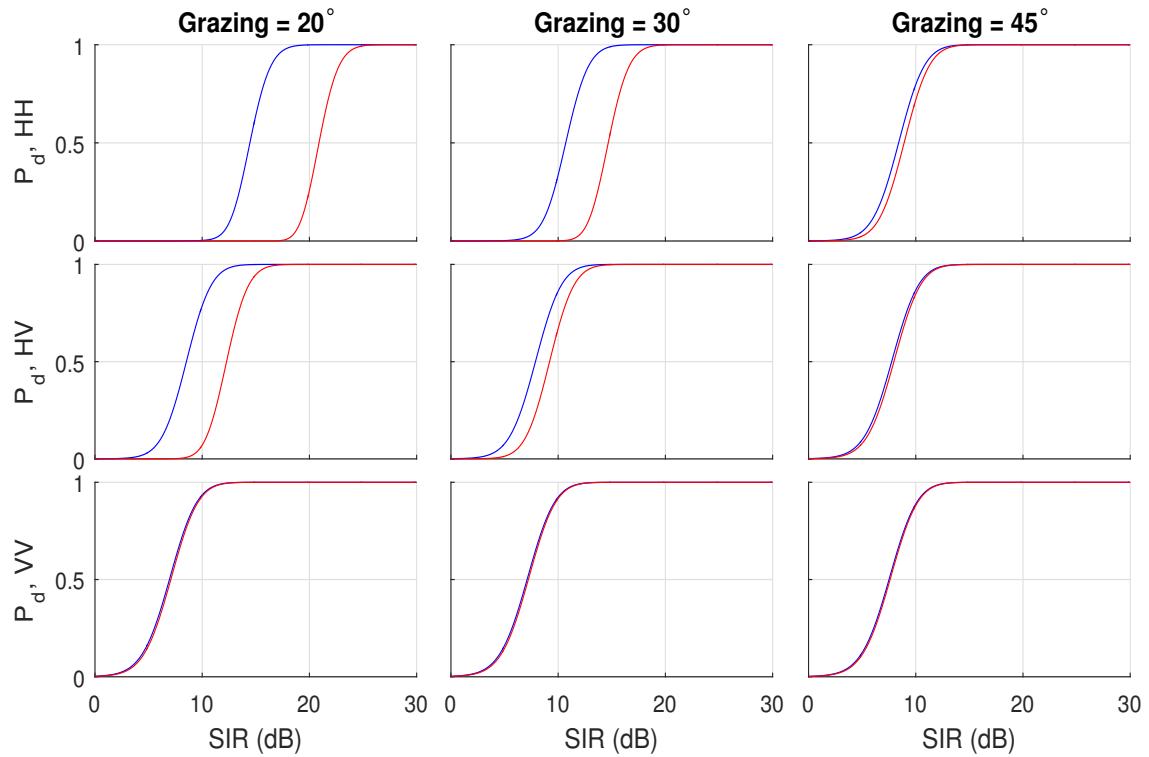
Figure 16: P_d variation with polarisation and grazing angle: (—) K, (—) Pareto.
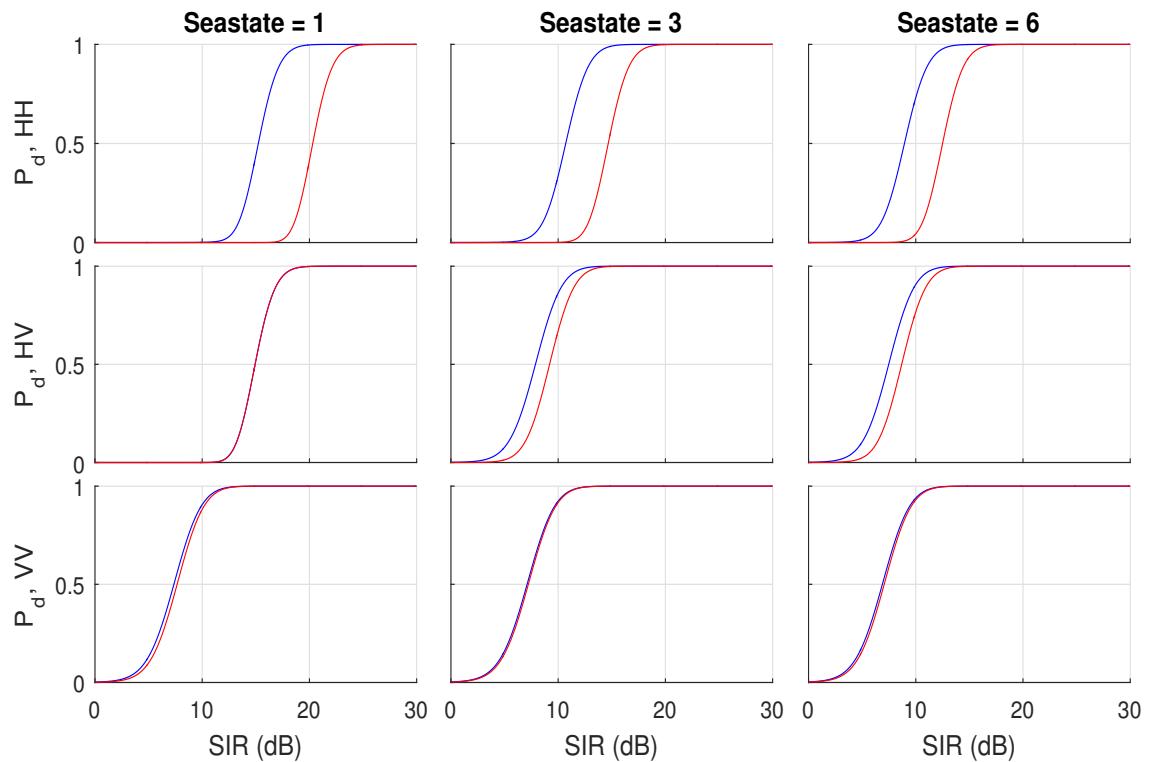
Figure 17: P_d variation with polarisation and sea-state: (—) K, (—) Pareto.

Table 13: Required SIR (dB) at a P_d of 0.5. Variation in grazing angle corresponding to Figure 16.

Pol.	$\theta = 20°$		$\theta = 30°$		$\theta = 45°$	
	K	Pareto	K	Pareto	K	Pareto
HH	14.45	20.89	10.71	14.67	8.40	8.91
HV	8.53	12.27	7.88	9.20	7.75	7.96
VV	6.94	7.07	7.10	7.22	7.51	7.61

Table 14: Required SIR (dB) at a P_d of 0.5. Variation in sea-state corresponding to Figure 17.

Pol.	$S = 1$		$S = 3$		$S = 6$	
	K	Pareto	K	Pareto	K	Pareto
HH	15.24	20.31	10.71	14.67	8.94	12.50
HV	14.93	14.93	7.88	9.20	7.48	8.69
VV	7.36	7.36	7.10	7.22	6.89	7.06

4.3 Minimum detectable target RCS

The final section looks at the the minimum detectable point target RCS for a given set of radar parameters and a desired P_{fa} and P_{d}. These can be related using the radar range equation as it applies to both the target and the sea-clutter. For the sea-clutter, the mean power was given in Equation 1. For the mean target power,

$$p_s = \frac{P_t G^2 \lambda_c^2 \sigma_t T_p B}{(4\pi)^3 R^4 L_a L_s} \tag{107}$$

where σ_t is the effective target RCS inclusive of any propagation effects. To determine the minimum detectable target RCS, $\sigma_{t,\text{min}}$, the relationship for the SIR can be used:

$$s = \frac{p_s}{p_c + p_n}. \tag{108}$$

If this relationship is then written in terms of the minimum detectable target RCS, $\sigma_{t,\text{min}}$,

$$\sigma_{t,\text{min}} = s_{0,\text{min}} \left(\sigma_c + \frac{k T_0 F_n (4\pi)^3 R^4 L_a L_s}{P_t G^2 \lambda_c^2 T_p} \right) \tag{109}$$

where $s_{0,\text{min}}$ is the minimum required SIR. Using the parameters given above, Figure 18 shows the minimum SIR and the corresponding minimum target RCS for each polarisation as it varies with grazing angle. Also shown in both results is the noise limited case ($p_c = 0$) which is constant at 3 dB for the minimum SIR and -14 dB for the minimum target RCS. For the lower grazing angles in the HH and HV channels, there is a large difference between the K and Pareto distributions, which reduces as the grazing angle increases. The two distributions give almost identical results for the VV channel. In terms of detectability, the Pareto result shows that the HV polarisation has the smallest target RCS, then VV and HH.
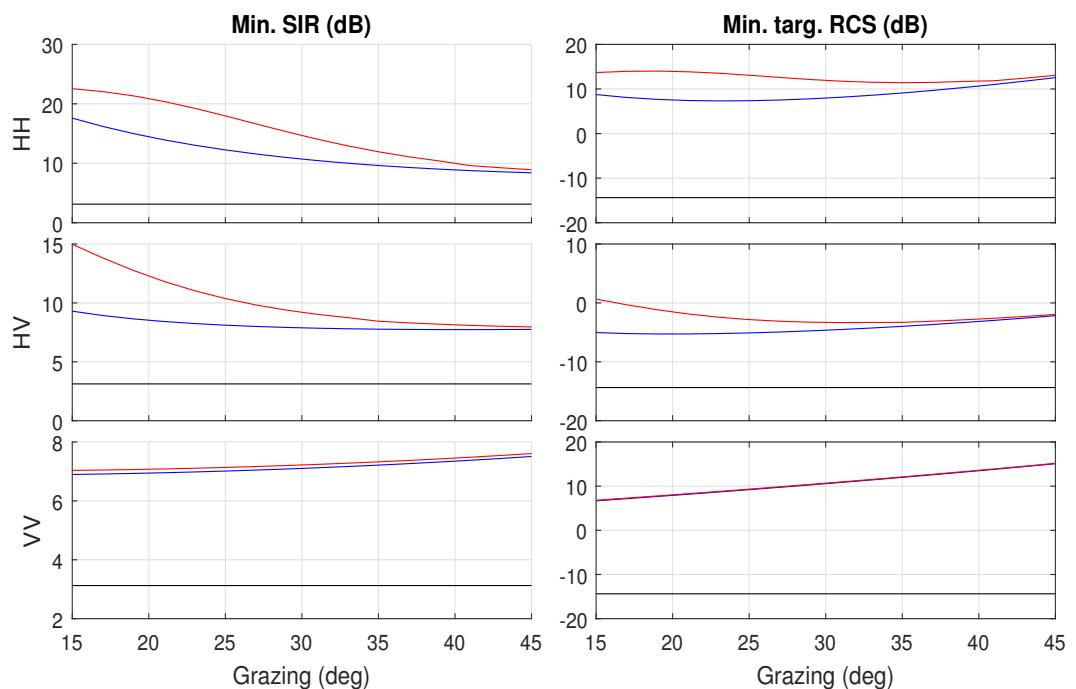
Figure 18: *Minimum required SIR (left) and minimum detectable target RCS (right) with $M = 10$ looks and $P_{fa} = 10^{-5}$. Other parameters given in Table 6: (—) K, (—) Pareto, (—) noise limited case.*

5   Conclusions and future work

Parametric modelling is a useful tool to predict a radar's target detection performance given a statistical description of the environment. This report summarised the target detection performance of an X-band surface surveillance radar operating at medium grazing angles in the maritime environment. A number of different detection scenarios were explored with variations in the collection geometry, sea-state and polarisation. Due to its good fit to the Ingara sea clutter data, the Pareto distribution was used as a proxy for the data with the K-distribution results showing the mismatch that would be expected in a detection scenario. The overwhelming conclusion from this report is that the choice of model is critical to accurately determine the detection performance.

These scenarios required a number of parameter models to relate the radar and environmental characteristics to the appropriate mean backscatter and the distribution shape values. Appropriate models were therefore presented along with the equations used to determine the performance of different fluctuating targets in both uncorrelated and correlated clutter. A full derivation of the Ward, Tough and Watts detection algorithm for correlated clutter was presented with a modification to make the technique robust for high CNRs.

The sea-clutter and target detection models were then used to analyse the probability of false alarm, probability of detection and the minimum detectable RCS for a given set of radar parameters. The P_{fa} results showed a a big difference in the horizontal polarisations with the K distribution underestimating the threshold by up to 5 dB, while there was only a minor difference in the VV channel. The effect of non-coherently integrating pulses was to reduce the threshold.

A comparison of the target fluctuation models revealed that the chi-squared distribution model has a slightly lower P_{d} than the exponential distribution and that increasing the target correlation reduced the slope. Using a distribution model also allows us to extrapolate down to lower P_{fa} levels than could be used in a real detection scheme. By comparing P_{fa} levels, it was found that for the HH polarisation, the difference in the SIR between the K and Pareto distributions was up to 5.4 dB. This mismatch also got larger as the P_{fa} reduced. When looking at changes in the azimuth look direction, the biggest variation between the K and Pareto distributions was found for the horizontal crosswind directions where the SIR difference was up to 7.7 dB. There was little difference in the VV polarisation, where the Pareto matched the K-distribution result. For changes in grazing, a difference was observed between the distribution models of up to 6.4 dB. The mismatch is reduced for the VV polarisation and also when the grazing gets higher. The final comparison was for the sea-state, where the largest mismatch of 5.1 dB is found for the lowest sea-state in the HH polarisation. The mismatch reduced as the sea-state increased and was very small for the VV polarisation.

The final result looked at the minimum detectable target RCS given a set of radar parameters. For the lower grazing angles in the HH and HV channels, there was a large difference between the K and Pareto distributions, which reduced as the grazing angle increased. In terms of detectability, the Pareto result shows that the VV polarisation has the smallest target RCS, then HV and HH.

These parameter models have also been recently used for simulating realistic sea-clutter with an evolving Doppler spectrum along time and range [Watts 2012, Watts, Rosenberg & Ritchie 2014, Bocquet, Rosenberg & Watts 2014]. By injecting false targets into this simulated data, detection performance can be analysed using adaptive CFAR algorithms and other 'new' detection schemes.

References

Allen, M. R. & Urkowitz, H. (1993) Radar detection performance limitations in sea-clutter for conventional noncoherent integration, *in IEEE National Radar Conference*, pp. 260–263.

Balleri, A., Nehorai, A. & Wang, J. (2007) Maximum likelihood estimation for compound-Gaussian clutter with inverse gamma texture, *IEEE Transactions on Aerospace and Electronic Systems* **43**(2), 775–779.

Barton, D. K. (1969) Simple procedures for radar detection calculations, *IEEE Transactions on Aerospace and Electronic Systems* **AES-5**(5), 837–846.

Bocquet, S. (2012) *Calculation of radar Probability of Detection in K Distributed Sea Clutter and Noise*, Technical Note DSTO-TN-1000, DSTO. Revised Edition.

Bocquet, S. (2015) Parameter estimation for Pareto and K distributed clutter with noise, *IET Radar Sonar and Navigation* **9**(1), 104–113.

Bocquet, S., Rosenberg, L. & Watts, S. (2014) Simulation of coherent sea clutter with inverse gamma texture, *in International Radar Conference*.

Briggs, J. N. (2004) *Target Detection by Marine Radar*, IEE Radar, Sonar and Navigation series 16, The Institution of Electrical Engineers.

Chernoff, H. (1952) A measure of asymptotic efficiency for tests of a hypothesis based on the sum of observations, *The Annals of Mathematical Statistics* **23**(4), 493–507.

Crisp, D. J., Kyprianou, R., Rosenberg, L. & Stacy, N. J. (2008) Modelling X-band sea clutter at moderate grazing angles, *in International Radar Conference*, pp. 596–601.

Crisp, D. J., Rosenberg, L. & Stacy, N. J. S. (2015) *Modelling ocean backscatter in the plateau region at X-band with the K-distribution*, Research report in preparation, DSTO.

Crisp, D. J., Stacy, N. J. & Goh, A. S. (2006) *Ingara Medium-High Incidence Angle Polarimetric Sea Clutter Measurements and Analysis*, Technical Report DSTO-TR-1818, DSTO.

Dong, Y. (2006) *Distribution of X-Band High Resolution and High Grazing Angle Sea Clutter*, Research Report DSTO-RR-0316, DSTO.

Edrington, T. S. (1965) The amplitude statistics of aircraft radar echoes, *IEEE Transactions on Military Electronics* **9**(1), 10–16.

Farina, A., Gini, F., Greco, M. V. & Lee, P. H. Y. (1996) Improvement factor for real sea-clutter Doppler frequency spectra, *IEE Proceedings of Radar, Sonar and Navigation* **143**(5), 341–344.

Farshchian, M. & Posner, F. L. (2010) The Pareto distribution for low grazing angle and high resolution X-band sea clutter, *in IEEE Radar Conference*, pp. 789–793.

Gradshteyn, I. S. & Ryzhik, I. M. (1994) *Tables of integrals, series and products*, 5 edn, Academic Press.

Hicks, N. L., Knable, N., Kovaly, J. J., Newell, G. S., Ruina, J. P. & Sherwin, C. W. (1960) The spectrum of X-band radiation backscattered from the sea surface, *Journal of Geophysical Research* **65**(3), 825–837.

Hou, X.-Y. & Morinaga, N. (1988) Detection performance of Rayleigh fluctuating targets in correlated Gaussian clutter plus noise, *The Transactions of the Institute of Electronics, Information and Communication Engineers (IEICE)* **E. 71**(3), 208–217.

Jakeman, E. & Pusey, P. N. (1976) A model for non-Rayleigh sea echo, *IEEE Transactions on Antennas and Propagation* **AP-24**(6), 806–814.

Kanter, I. (1986) Exact detection probability for partially correlated Rayleigh targets, *IEEE Transactions on Aerospace and Electronic Systems* **AES-22**(2), 184–196.

Kotz, S. & Neumann, J. (1963) On the distribution of precipitation amounts for periods of increasing length, *Journal of Geophysical Research* **68**(12), 3635–3640.

Lamont-Smith, T. (2000) Translation to the normal distribution for radar clutter, *IEE Proceedings of Radar, Sonar and Navigation* **147**(1), 17–22.

Lee, P. H. Y., Barter, J. D., Caponi, E., Hidman, C. L., Lake, B. M., Rungaldier, H. & Shelton, J. C. (1995) Power spectral lineshapes of microwave radiation backscattered from sea surfaces at small grazing angles, *IEE Proceedings of Radar, Sonar and Navigation* **142**(5), 252–258.

Long, M. W. (2001) *Radar Reflectivity of Land and Sea - Third Edition*, Artech House.

Marcum, J. L. (1960) A statistical theory of target detection by pulsed radar, *IRE Transactions* **IT-6**, 59–144.

Masuko, H., Okamoto, K., Shimada, M. & Niwa, S. (1986) Measurement of microwave backscattering signatures of the ocean surface using X band and Ka band airborne scatterometers, *Geophysical Research* **91**(C11), 13065–13083.

Meyer, D. P. & Mayer, H. A. (1973) *Radar Target Detection*, Academic Press.

Middleton, D. (1999) New physical-statistical methods and model for clutter and reverberation: The KA-distribution and related probability structures, *IEEE Journal of Oceanic Engineering* **24**(3), 261–284.

Nandagopal, M., Sen, S. & Rawat, A. (2010) A note on the error function, *Computing Prescriptions* pp. 84–88.

Pearson, J. (2009) *Computation of Hypergeometric Functions*, Masters thesis, University of Oxford.

Plant, W. J. (1997) A model for microwave Doppler sea return at high incidence angles: Bragg scattering from bound, tilted waves, *Journal of Geophysical Research* **102**(C9), 21,131–21,146.

Rosenberg, L. (2012) The effect of temporal correlation with K and KK-distributed sea-clutter, *in IEEE Radar Conference*, pp. 303–308.

Rosenberg, L. (2013) Sea-spike detection in high grazing angle X-band sea-clutter, *IEEE Transactions on Geoscience and Remote Sensing* **51**(8), 4556–4562.

Rosenberg, L. (2014) Characterisation of high grazing angle X-band sea-clutter Doppler spectra, *IEEE Transaction on Aerospace and Electronic Systems* **50**(1), 406–417.

Rosenberg, L. & Bocquet, S. (2013*a*) The Pareto distribution for high grazing angle sea-clutter, *in IEEE Proceedings on Geoscience and Remote Sensing*, pp. 4209–4212.

Rosenberg, L. & Bocquet, S. (2013*b*) Robust performance prediction modelling for compound distributions with temporal correlation, *in International Radar Conference*, pp. 388–393.

Rosenberg, L. & Bocquet, S. (2015) Application of the Pareto plus noise distribution to medium grazing angle sea-clutter, *IEEE Journal of Selected Topics in Applied Earth Observations and Remote Sensing* **8**(1), 255–261.

Rosenberg, L. & Crisp, D. (2010*a*) X-band performance with medium grazing angle sea-clutter, *in European SAR Conference*, pp. 669–672.

Rosenberg, L., Crisp, D. J. & Stacy, N. J. (2009) Statistical models for medium grazing angle X-band sea-clutter, *in Defence Applications of Signal Processing*.

Rosenberg, L., Crisp, D. J. & Stacy, N. J. (2010*b*) Analysis of the KK-distribution with medium grazing angle sea-clutter, *IET Proceedings of Radar Sonar and Navigation* **4**(2), 209–222.

Rosenberg, L., Watts, S. & Bocquet, S. (2014) Application of the K+Rayleigh distribution to high grazing angle sea-clutter, *in International Radar Conference*.

Rosenberg, L., Watts, S., Bocquet, S. & Ritchie, M. (2015) Characterisation of the Ingara HGA dataset, *in International Radar Conference*.

Shimada, T., Kawamura, H. & Shimada, M. (2003) An L-band geophysical model function for SAR wind retrieval using JERS-1 SAR, *IEEE Transactions on Geoscience and Remote Sensing* **41**(3), 518–531.

Shnidman, D. A. (1976) Efficient evaluation of the probabilities of detection and the generalized Q-function, *IEEE Transactions on Information Theory* **22**, 746–751.

Shnidman, D. A. (1989) The calculation of the probability of detection and the generalized Marcum Q-function, *IEEE Transactions on Information Theory* **35**(2), 389–400.

Shnidman, D. A. (1991) Note on 'the calculation of the probability of detection and the generalised Marcum Q-function', *IEEE Transactions on Information Theory* **35**, 1233.

Shnidman, D. A. (1995) Radar detection probabilities and their calculation, *IEEE Transactions on Aerospace and Electronic Systems* **31**(3), 928–950.

Shnidman, D. A. (1999) Generalized radar clutter model, *IEEE Transactions on Aerospace and Electronic Systems* **35**(3), 857–865.

Shnidman, D. A. (2005) Comparison of low angle radar clutter models, *IEEE Transactions on Aerospace and Electronic Systems* **41**(2), 736–746.

Skolnik, M. I. (2008) *Radar Handbook*, 3 edn, McGraw-Hill.

Spaulding, B., Horton, D. & Pham, H. (2005) Wind aspect factor in sea clutter modeling, *in International Radar Conference*, pp. 89–92.

Swerling, P. (1960) Probability of detection for fluctuating targets, *IRE Transactions* **IT-6**, 269–308.

Swerling, P. (1970) Recent developments in target models for radar detection analysis, *in AGARD Avionics Technical Symposium Proceedings*, Istanbul, Turkey.

Technology Service Corporation (1990) Backscatter from sea, *Radar Workstation* **2**, 177–186.

Ulaby, F. T., Moore, R. K. & Fung, A. K. (1982) *Microwave Remote Sensing: Active and Passive, Volume II: Radar Remote Sensing and Surface Scattering and Emission Theory*, Addison-Wesley.

Walker, D. (2001) Doppler modelling of radar sea clutter, *IEE Proceedings of Radar, Sonar and Navigation* **148**(2), 73–80.

Ward, K. D. (1981) Compound representation of high resolution sea clutter, *Electronic Letters* **17**(16), 561–563.

Ward, K. D. & Tough, R. J. A. (2002) Radar detection performance in sea clutter with discrete spikes, *in International Radar Conference*, pp. 15–17.

Ward, K. D., Tough, R. J. A. & Watts, S. (2013) *Sea Clutter: Scattering, the K-Distribution and Radar Performance*, second edn, The Institute of Engineering Technology.

Watts, S. (2012) Modeling and simulation of coherent sea clutter, *IEEE Transactions on Aerospace and Electronic Systems* **48**(4), 3303–3317.

Watts, S., Rosenberg, L. & Ritchie, M. (2014) Characterising the Doppler spectra of high grazing angle sea clutter, *in International Radar Conference*.

Weinberg, G. V. (2011*a*) Assessing Pareto fit to high-resolution high-grazing-angle sea clutter, *IET Electronic Letters* **4747**(8), 516–517.

Weinberg, G. V. (2011*b*) *An Investigation of the Pareto Distribution as a Model for High Grazing Angle Clutter*, Technical Report DSTO-TR-2525, DSTO.

Weinberg, G. V. (2012*a*) *Coherent Multilook Radar Detection for Targets in KK Distributed Clutter*, InTech, chapter 9, pp. 161–176.

Weinberg, G. V. (2012*b*) *Coherent Multilook Radar Detection for Targets in Pareto Distributed Clutter*, Technical Report DSTO-TR-2646, DSTO.

Weinberg, G. V. (2014) Examination of classical detection schemes for targets in Pareto distributed clutter: Do classical CFAR detectors exist, as in the Gaussian case?, *Multidimensional Systems and Signal Processing* **25**(1), 1–19.

Weiner, M. A. (1988) Detection probability for partially correlated Chi-square targets, *IEEE Transactions on Aerospace and Electronic Systems* **24**(4), 411–416.

Weinstock, W. (1964) *Target cross section models for radar system analysis*, PhD thesis, University of Pennsylvania.

Wozencraft, J. M. & Jacobs, I. M. (1965) *Principles of Communication Engineering*, John Wiley and Sons.

Appendix A   PDFs for correlated clutter

This appendix derives the PDFs from the WTW detection model in Section 3.3.2 for the cases of correlated clutter and noise and a target in correlated clutter and noise. The PDFs derived below are for clutter speckle, so numerical integration over the texture PDF is required to obtain the PDF for compound clutter, as described in Section 3.4. In order to obtain accurate results for both low and high intensity, the integration interval is separated into two parts, with 100 point Gauss-Legendre quadrature used on $[0, 1]$ and 20 point Gauss-Laguerre quadrature on $[1, \infty)$.

A.1   Correlated clutter and noise

The PDF for correlated clutter and noise is evaluated as follows. With no target present, $\tilde{s} = 0$ and Equation 70 becomes

$$P(\beta|\alpha, L) = \frac{\beta^{L-1}\alpha^{-L}e^{-\beta/\alpha}}{\Gamma(L)}. \tag{A1}$$

The PDF can then be written as

$$
\begin{aligned}
P(\tilde{\mu}|M, L, \alpha) &= \int_0^\infty P(\tilde{\mu}|\beta, M)P(\beta|\alpha, L)d\beta \\
&= \frac{\alpha^{-L}}{\Gamma(L)}\sum_{k=0}^\infty \frac{e^{-\tilde{\mu}}\tilde{\mu}^{M+k-1}}{k!(M+k-1)!}\int_0^\infty \exp\left(-\frac{\beta(\alpha+1)}{\alpha}\right)\beta^{k+L-1}d\beta \\
&= \sum_{k=0}^\infty \frac{\Gamma(L+k)e^{-\tilde{\mu}}\tilde{\mu}^{M+k-1}\alpha^k}{\Gamma(L)k!(M+k-1)!(\alpha+1)^{L+k}} \\
&= \frac{e^{-\tilde{\mu}}\tilde{\mu}^{M-1}}{\Gamma(M)(\alpha+1)^L}\sum_{k=0}^\infty \frac{\Gamma(L+k)\Gamma(M)}{k!\Gamma(L)\Gamma(M+k)}\left(\frac{\alpha\tilde{\mu}}{\alpha+1}\right)^k \\
&= \frac{e^{-\tilde{\mu}}\tilde{\mu}^{M-1}}{\Gamma(M)(\alpha+1)^L}\,{}_1F_1\left(L; M; \frac{\alpha\tilde{\mu}}{\alpha+1}\right) \tag{A2}
\end{aligned}
$$

and is the same PDF obtained by [Swerling 1970, Equation 54] for a fluctuating target in noise. It is also the 'noncentral chi-square gamma' PDF used by Shnidman [1999] as a clutter model. The confluent hypergeometric function can be evaluated using a Taylor series for small arguments and an asymptotic series for large arguments [Pearson 2009]. Here the parameters and argument are all positive and real or integer, so the function is also real and positive with no singularities. In this case, the asymptotic series can be simplified to

$$
{}_1F_1(L; M; u) = \frac{\Gamma(N)}{\Gamma(L)}u^{L-N}e^u\sum_{k=0}^\infty \frac{(M-L)_k(1-L)_k}{k!}u^{-k}. \tag{A3}
$$

The asymptotic series is used for $u \geq 100$, and the Taylor series for $u < 100$. If the MATLAB symbolic math toolbox is available, the function 'hypergeom' could be used, but according to [Pearson 2009], this function is at least 100 times slower than direct evaluation of the series. The PDF is obtained by numerical integration of Equation A2 over the gamma distribution for the clutter power x. The dependence on x is only through the parameter α, per Equation 69.

Figure A1 shows the PDF for $M = 10$ pulses and different values of L, with a CNR of 0 dB and K distribution shape parameter $\nu = 0.1$. The clutter correlation mainly affects the tail of the distribution, and hence the probability of false alarm for a given threshold.
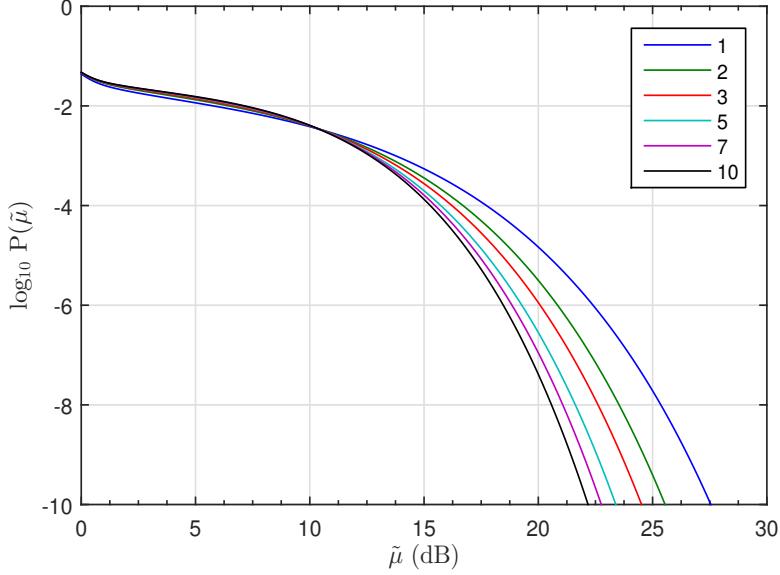
Figure A1: PDF for the sum of 10 returns from correlated K clutter and noise, with a CNR of 0 dB and shape parameter ν = 0.1, for different numbers of independent clutter samples.

A.2 Target in correlated clutter and noise

The PDF for a target in correlated clutter and noise is

$$P(\tilde{\mu}|M, L, \alpha, \tilde{S}, K) = \int_0^\infty \int_0^\infty P(\tilde{\mu}|\beta, M) P(\beta|\tilde{s}, \alpha, L) P(\tilde{s}|\tilde{S}, K) d\beta d\tilde{s}. \tag{A4}$$

The integral over β can be evaluated using the definite integral [Gradshteyn & Ryzhik 1994, §6.633]:

$$\int_0^\infty x^{p+1} e^{-qx^2} J_m(fx) J_n(gx) dx = \frac{f^m g^n q^{-(m+n+p+2)/2}}{2^{m+n+1}\Gamma(n+1)}$$

$$\times \sum_{k=0}^\infty \frac{\Gamma(k + (m+n+p+2)/2)}{k!\Gamma(k+m+1)} \left(-\frac{f^2}{4q}\right)^k {}_2F_1\left(-k, -m-k; n+1; \frac{g^2}{f^2}\right) \tag{A5}$$

If we make the substitutions

$$\begin{aligned} x &= \sqrt{\beta}, \quad dx = \frac{d\beta}{2\sqrt{\beta}}, \\ f &= jF, \qquad g = jG, \\ p &= m - n, \end{aligned} \tag{A6}$$

then Equation A5 can be written as

$$\int_0^\infty \beta^{(m-n)/2} e^{-q\beta} I_m\left(F\sqrt{\beta}\right) I_n\left(G\sqrt{\beta}\right) d\beta$$

$$= \frac{F^m G^n q^{-m-1}}{2^{m+n}\Gamma(n+1)} \sum_{k=0}^\infty \frac{1}{k!} \left(-\frac{F^2}{4q}\right)^k {}_2F_1\left(-k, -m-k; n+1; \frac{G^2}{F^2}\right). \tag{A7}$$

If the target is non-fluctuating, $\tilde{s} = \tilde{S}$, and the definite integral from Equation A7 can be applied to obtain the PDF

$$
\begin{aligned}
P(\tilde{\mu}|M, L, \alpha, \tilde{S}) &= \int_0^\infty P(\tilde{\mu}|\beta, M) P(\beta|\tilde{S}, \alpha, L) d\beta \\
&= \frac{\tilde{\mu}^{(M-1)/2} \exp\left(-\tilde{\mu} - \tilde{S}/\alpha\right)}{\alpha \tilde{S}^{(L-1)/2}} \\
&\quad \times \int_0^\infty \beta^{(L-M)/2} \exp\left(-\frac{\beta(\alpha+1)}{\alpha}\right) I_{M-1}\left(2\sqrt{\tilde{\mu}\beta}\right) I_{L-1}\left(\frac{2\sqrt{\tilde{S}\beta}}{\alpha}\right) d\beta \\
&= \frac{\tilde{\mu}^{M-1} \exp\left(-\tilde{\mu} - \tilde{S}/\alpha\right)}{\Gamma(M)(\alpha+1)^L} \sum_{k=0}^\infty \frac{1}{k!}\left(\frac{\tilde{S}}{\alpha+1}\right)^k {}_2F_1\left(-k, -L-k+1; M; \frac{\alpha\tilde{\mu}}{\tilde{S}}\right) \\
&= \frac{\tilde{\mu}^{M-1} \exp\left(-\tilde{\mu} - \tilde{S}/\alpha\right)}{\Gamma(M)(\alpha+1)^L} \sum_{k=0}^\infty \frac{1}{k!}\left(\frac{\tilde{S}}{\alpha+1}\right)^k \sum_{m=0}^k \frac{(L)_m}{(M)_m}\left(\frac{\alpha\tilde{\mu}}{\tilde{S}}\right)^m \\
&= \frac{\tilde{\mu}^{M-1} \exp\left(-\tilde{\mu} - \tilde{S}/\alpha\right)}{\Gamma(M)(\alpha+1)^L} \sum_{k=0}^\infty \frac{1}{k!}\left(\frac{\alpha\tilde{\mu}}{\alpha+1}\right)^k \sum_{m=0}^k \frac{(L)_m}{(M)_m}\left(\frac{\tilde{S}}{\alpha\tilde{\mu}}\right)^{k-m}.
\end{aligned} \tag{A8}
$$

If there is no target present, $\tilde{S} = 0$ and Equation A8 reduces to Equation A2. For a fluctuating target the PDF is

$$
\begin{aligned}
P(\tilde{\mu}|M, L, \alpha, \tilde{S}, K) &= \int_0^\infty P(\tilde{\mu}|M, L, \alpha, \tilde{s}) P(\tilde{s}|\tilde{S}, K) d\tilde{s} \\
&= \frac{\tilde{\mu}^{M-1} e^{-\tilde{\mu}}}{\Gamma(M)(\alpha+1)^L} \sum_{k=0}^\infty \frac{1}{k!(\alpha+1)^k} \sum_{m=0}^k \frac{(L)_m}{(M)_m}(\alpha\tilde{\mu})^m \frac{\left(K/\tilde{S}\right)^K}{\Gamma(K)} \\
&\quad \times \int_0^\infty \tilde{s}^{K+k-m-1} \exp\left(-\tilde{s}\left(\frac{\tilde{S} + \alpha K}{\alpha\tilde{S}}\right)\right) d\tilde{s} \\
&= \frac{\tilde{\mu}^{M-1} e^{-\tilde{\mu}} \left(K/\tilde{S}\right)^K}{\Gamma(M)(\alpha+1)^L} \sum_{k=0}^\infty \frac{1}{k!(\alpha+1)^k} \\
&\quad \times \sum_{m=0}^k \frac{(L)_m (K)_{k-m}}{(M)_m}\left(\frac{\alpha\tilde{S}}{\tilde{S} + \alpha K}\right)^{K+k-m}(\alpha\tilde{\mu})^m.
\end{aligned} \tag{A9}
$$

Appendix B   WTW detection model consistency check

This appendix presents a consistency check for the WTW detection model to show that in the case of a non-fluctuating target, the M pulse Rice distribution is recovered when the effective number of looks L equals the number of pulses M. This can be verified by integrating the product of the PDFs in Equations 70 and 72 over β,

$$
\begin{aligned}
P(\tilde{\mu}|\tilde{s}, \alpha, M) &= \int_0^\infty P(\tilde{\mu}|\beta, M) P(\beta|\tilde{s}, \alpha, M) d\beta \\
&= \left(\frac{\tilde{\mu}}{\tilde{s}}\right)^{(M-1)/2} \frac{\exp\left(-\tilde{\mu} - \tilde{s}/\alpha\right)}{\alpha} \\
&\quad \times \int_0^\infty \exp\left(-\beta \frac{\alpha + 1}{\alpha}\right) I_{M-1}\left(2\sqrt{\tilde{\mu}\beta}\right) I_{M-1}\left(\frac{2\sqrt{\tilde{s}\beta}}{\alpha}\right) d\beta
\end{aligned}
\tag{B1}
$$

where the integral in Equation B1 can be evaluated using [Gradshteyn & Ryzhik 1994, §6.615]:

$$
\int_0^\infty e^{-px} J_m\left(2f\sqrt{x}\right) J_m\left(2g\sqrt{x}\right) dx = \frac{1}{p} I_m\left(\frac{2fg}{p}\right) \exp\left(-\frac{f^2 + g^2}{p}\right).
\tag{B2}
$$

By making the following substitutions: $f = jF = e^{\frac{\pi}{2}j} F$ and $g = jG = e^{\frac{\pi}{2}j} G$ and noting that $I_m(z) = e^{-m\frac{\pi}{2}j} J_m\left(e^{\frac{\pi}{2}j} z\right)$ [Gradshteyn & Ryzhik 1994, §8.406/1], and $I_m(-z) = I_m\left(e^{\pi j} z\right) = e^{m\pi j} I_m(z)$ from the series [Gradshteyn & Ryzhik 1994, §8.445], Equation B2 can be written as

$$
\int_0^\infty e^{-px} I_m\left(2F\sqrt{x}\right) I_m\left(2G\sqrt{x}\right) dx = \frac{1}{p} I_m\left(\frac{2FG}{p}\right) \exp\left(\frac{F^2 + G^2}{p}\right).
\tag{B3}
$$

Hence

$$
\begin{aligned}
P(\tilde{\mu}|\tilde{s}, \alpha, M) &= \left(\frac{\tilde{\mu}}{\tilde{s}}\right)^{(M-1)/2} \frac{e^{-\tilde{\mu} - \tilde{s}/\alpha}}{\alpha + 1} I_{N-1}\left(\frac{2\sqrt{\tilde{\mu}\tilde{s}}}{\alpha + 1}\right) \exp\left(\frac{\alpha\left(\tilde{\mu} + \tilde{s}/\alpha^2\right)}{\alpha + 1}\right) \\
&= \frac{1}{\alpha + 1} \left(\frac{\tilde{\mu}}{\tilde{s}}\right)^{(M-1)/2} \exp\left(-\frac{\tilde{\mu} + \tilde{s}}{\alpha + 1}\right) I_{M-1}\left(\frac{2\sqrt{\tilde{\mu}\tilde{s}}}{\alpha + 1}\right).
\end{aligned}
\tag{B4}
$$

The Rice distribution for the sum μ of M radar returns from a target in noise and uncorrelated clutter speckle was given in Equation 49 as

$$
P(\mu|s, M) = \left(\frac{\mu}{s}\right)^{(M-1)/2} e^{-(\mu+s)} I_{M-1}\left(2\sqrt{\mu s}\right)
\tag{B5}
$$

and since $\alpha = x/p_n$ when $L = M$, we have $\mu = \tilde{\mu}/(\alpha + 1)$ and $s = \tilde{s}/(\alpha + 1)$. Then by comparing Equation B4 with Equation B5, it can be seen that $P(\tilde{\mu}|\tilde{s}, \alpha, M) d\tilde{\mu} = P(\mu|s, M) d\mu$.

Appendix C   Calculation bounds for the WTW detection probability

This appendix supplements the WTW algorithm description in Sections 3.3.2 and 3.3.3. Section C.1 describes the Chernoff bounds which are used to detect cases when the P_d is less than the minimum value that can be represented on a computer or when $1 - P_\mathrm{d}$ is less than the smallest number which can be represented with double precision and the best solutions will be either 0 or 1 respectively. Section C.2 then derives practical lower and upper limits for evaluating the P_d in Equation 87.

C.1   Chernoff bounds

Chernoff bounds provide a means to avoid unnecessary calculations when the probability of detection is close to zero or one [Chernoff 1952, Wozencraft & Jacobs 1965, Shnidman 1976, Shnidman 1995, Bocquet 2012]. They are a function of the number of looks, M, the SIR, $\tilde{S}$, the threshold, $\tilde{\tau}$ and a parameter, λ. If an upper bound is desired, then the value of λ must be found which most closely matches the inequality

$$P_\mathrm{d}(M, \tilde{S}, \tilde{\tau}) \leq C_B(M, \tilde{S}, \tilde{\tau}, \lambda) \qquad \text{(C1)}$$

or for a lower bound

$$P_\mathrm{d}(M, \tilde{S}, \tilde{\tau}) \geq 1 - C_B(M, \tilde{S}, \tilde{\tau}, \lambda). \qquad \text{(C2)}$$

To use the Chernoff bound, the optimal λ_0 is calculated for the appropriate target model and two cases are investigated:

λ_0 **is positive** implies P_d is less than $C_B(M, \tilde{S}, \tilde{\tau}, \lambda_0)$ and we set P_d to 0.

λ_0 **is negative** implies P_d is greater than $C_B(M, \tilde{S}, \tilde{\tau}, \lambda_0)$, and we set P_d to 1.

When applied to the compound distributions, the Chernoff bounds are calculated prior to numerical integration for each value of α used in the integration. In MATLAB, this can be done simultaneously by treating the variable α as a vector formed from all the required values. Even though the calculation of λ_0 is rather complicated, evaluation of the Chernoff bound is generally much faster than summing the series for the probability of detection, especially for large $\tilde{\tau}$ where many terms are needed for the series to converge.

Non-fluctuating target in uncorrelated clutter

For a non-fluctuating target in noise, the Chernoff bound is [Shnidman 1995, Equation 73]

$$C_B(M, \tilde{S}, \tilde{\tau}, \lambda) = \frac{\exp(-\lambda\tilde{\tau} + \tilde{S}\lambda/(1 - \lambda))}{(1 - \lambda)^M}. \qquad \text{(C3)}$$

Non-fluctuating target in correlated clutter

The bound for an effective number of looks L in correlated clutter plus noise is obtained by setting $\tilde{S} = \beta$ and integrating over the probability $P(\beta|\tilde{S}, \alpha, L)$:

$$
\begin{aligned}
C_B(M, L, \alpha, \tilde{S}, \tilde{\tau}, \lambda) &= \int_0^\infty C_B(M, \beta, \tilde{\tau}, \lambda) P(\beta|\tilde{S}, \alpha, L) d\beta \\
&= \int_0^\infty \frac{\exp(-\lambda\tilde{\tau} + \beta\lambda/(1-\lambda))}{(1-\lambda)^M} \frac{1}{\alpha} \left(\frac{\beta}{\tilde{S}}\right)^{\frac{L-1}{2}} \exp\left(-\frac{\beta + \tilde{S}}{\alpha}\right) I_{L-1}\left(\frac{2\sqrt{\beta\tilde{S}}}{\alpha}\right) d\beta \\
&= \frac{\exp\left(-\lambda\tilde{\tau} - \tilde{S}/\alpha\right)}{\alpha(1-\lambda)^M} \int_0^\infty \exp(-\beta(\lambda/(\lambda-1) + 1/\alpha)) \left(\frac{\beta}{\tilde{S}}\right)^{\frac{L-1}{2}} I_{L-1}\left(\frac{2\sqrt{\beta\tilde{S}}}{\alpha}\right) d\beta \\
&= \frac{\exp(-\lambda\tilde{\tau} + \tilde{S}\lambda/(1-\lambda-\alpha\lambda))}{(1-\lambda)^M} \left(\frac{1-\lambda}{1-\lambda-\alpha\lambda}\right)^L .
\end{aligned}
\tag{C4}
$$

The value of λ which gives the closest bound is then obtained by solving

$$
\frac{d\ln(C_B)}{d\lambda} = -\tilde{\tau} + \frac{\tilde{S}}{(1-\lambda-\alpha\lambda)^2} + \frac{M}{1-\lambda} + \frac{L\alpha}{(1-\lambda)(1-\lambda-\alpha\lambda)} = 0
\tag{C5}
$$

for λ. This result can be rearranged to form a cubic in λ

$$
t\lambda^3 + u\lambda^2 + v\lambda + w = 0
\tag{C6}
$$

with the coefficients

$$
\begin{aligned}
t &= \tilde{\tau}(1+\alpha)^2, \\
u &= (1+\alpha)\left((1+\alpha)M - (3+\alpha)\tilde{\tau}\right), \\
v &= \tilde{\tau}(3+2\alpha) - (1+\alpha)(2M+\alpha L) - \tilde{S}, \\
w &= \alpha L + M + \tilde{S} - \tilde{\tau}.
\end{aligned}
\tag{C7}
$$

Equation C6 can then be solved using radicals. Dividing through by t and making the substitution $\lambda = \eta - u/(3t)$ gives the equation

$$
\begin{aligned}
&\eta^3 + p\eta + q = 0 \text{ where} \\
&p = \frac{v}{t} - \frac{u^2}{3t^2} \text{ and} \\
&q = \frac{2u^3}{27t^3} - \frac{uv}{3t^2} + \frac{w}{t}.
\end{aligned}
\tag{C8}
$$

with a discriminant

$$
d = (q/2)^2 + (p/3)^3 .
\tag{C9}
$$

If $d > 0$, there is one real root

$$
\lambda_0 = \sqrt[3]{\frac{1}{2}\left(-q + \sqrt{d}\right)} + \sqrt[3]{\frac{1}{2}\left(-q - \sqrt{d}\right)} - u/(3t).
\tag{C10}
$$

If $d = 0$, there are three real roots given by

$$
\begin{aligned}
&\lambda_0 = 2r\cos\left(\frac{\phi + 2\pi}{3}\right) - \frac{u}{3t} \\
&\text{where } r = \sqrt{-p/3} \text{ and } \phi = \cos^{-1}\left(-\frac{q}{2r^3}\right).
\end{aligned}
\tag{C11}
$$

If $w < 0$, or $\tilde{\tau} > \alpha L + M + \tilde{S}$, then $\lambda_0 > 0$ and the result is an upper bound for the probability of detection near zero. Alternatively if $w > 0$, or $\tilde{\tau} < \alpha L + M + \tilde{S}$, then $\lambda_0 < 0$ and the bound is a lower bound for the probability of detection near one.

Fluctuating target in correlated clutter

The Chernoff bound for a fluctuating target is obtained by integrating the bound for a fixed target in Equation C4 with the fluctuation $P(\tilde{s}|\tilde{S}, K)$,

$$
\begin{aligned}
C_B(M, L, \alpha, \tilde{S}, K, \tilde{\tau}, \lambda) &= \int_0^\infty C_B(M, L, \alpha, \tilde{s}, \tilde{\tau}, \lambda) P(\tilde{s}|\tilde{S}, K) d\tilde{s} \\
&= \int_0^\infty \frac{\exp\left(-\lambda\tilde{\tau} + \frac{\tilde{s}\lambda}{1-\lambda-\alpha\lambda}\right)}{(1-\lambda)^M} \left(\frac{1-\lambda}{1-\lambda-\alpha\lambda}\right)^L \frac{\tilde{s}^{K-1}}{\Gamma(K)} \left(\frac{K}{\tilde{S}}\right)^K e^{-Ks/\tilde{S}} d\tilde{s} \\
&= \frac{e^{-\lambda\tilde{\tau}}}{(1-\lambda)^M} \left(\frac{1-\lambda}{1-\lambda-\alpha\lambda}\right)^L \frac{1}{\Gamma(K)} \left(\frac{K}{\tilde{S}}\right)^K \\
&\quad \times \int_0^\infty \tilde{s}^{K-1} \exp\left(-Ks/\tilde{S} + \frac{\tilde{s}\lambda}{1-\lambda-\alpha\lambda}\right) d\tilde{s} \\
&= \frac{e^{-\lambda\tilde{\tau}}}{(1-\lambda)^M} \left(\frac{1-\lambda}{1-\lambda-\alpha\lambda}\right)^L \left(\frac{K}{\tilde{S}}\right)^K \left(\frac{K}{\tilde{S}} - \frac{\lambda}{1-\lambda-\alpha\lambda}\right)^{-K} \\
&= \frac{e^{-\lambda\tilde{\tau}}}{(1-\lambda)^M} \left(\frac{1-\lambda}{1-\lambda-\alpha\lambda}\right)^L \left(1 - \frac{\tilde{S}}{K}\frac{\lambda}{1-\lambda-\alpha\lambda}\right)^{-K}. \quad \text{(C12)}
\end{aligned}
$$

The value of λ which gives the closest bound is obtained by solving

$$
\frac{d\ln(C_B)}{d\lambda} = -\tilde{\tau} + \frac{M}{1-\lambda} + \frac{L\alpha}{(1-\lambda)(1-\lambda-\alpha\lambda)} + \frac{\tilde{S}}{(1-\lambda-\alpha\lambda)\left(1-\lambda\left(1+\alpha+\tilde{S}/K\right)\right)} = 0 \quad \text{(C13)}
$$

which can be rearranged to form a cubic in λ with the coefficients

$$
\begin{aligned}
t &= \tilde{\tau}(1+\alpha)(1+\alpha+\tilde{S}/K), \\
u &= M(1+\alpha)(1+\alpha+\tilde{S}/K) - \tilde{\tau}(2+\alpha)(1+\alpha+\tilde{S}/K) - \tilde{\tau}(1+\alpha), \\
v &= \tilde{\tau}(3+2\alpha) - \alpha L(1+\alpha+\tilde{S}/K) - 2M(1+\alpha) - \tilde{S} + (\tilde{\tau} - M)\tilde{S}/K, \\
w &= \alpha L + M + \tilde{S} - \tilde{\tau}.
\end{aligned} \quad \text{(C14)}
$$

The solution for λ_0 is the same as the fixed target case (Equations C10 and C11), albeit with the coefficients in Equation C14 replacing those in Equation C7. Note that the coefficients for the fluctuating target reduce to those for the constant target in the limit $K \to \infty$.

Probability of false alarm

The Chernoff bound for the probability of false alarm is

$$
C_{B0}(M, L, \alpha, \tilde{\tau}, \lambda) = \frac{e^{-\lambda\tilde{\tau}}}{(1-\lambda)^M} \left(\frac{1-\lambda}{1-\lambda-\alpha\lambda}\right)^L \quad \text{(C15)}
$$

which is obtained by setting $\tilde{S} = 0$ in Equations C4 or C12. In this case the equation for the value of λ which gives the closest bound is a quadratic $\lambda^2 + p\lambda + q = 0$ with coefficients

$$
\begin{aligned}
p &= \frac{M}{\tilde{\tau}} - \frac{\alpha + 2}{\alpha + 1}, \\
q &= \frac{1 - (M + \alpha L)/\tilde{\tau}}{\alpha + 1}
\end{aligned}
\tag{C16}
$$

and the desired solution

$$
\lambda_0 = \left(-p - \sqrt{p^2 - 4q} \right) / 2.
\tag{C17}
$$

C.2 Calculation limits

This section derives the lower and upper limits for calculation of the detection probability in Equation 87. These bounds are important as an underflow problem arises when the threshold, $\tilde{\tau}$ is large in the $e^{-\tilde{\tau}} \tilde{\tau}^m / m!$ terms of Equation 74. As explained in [Bocquet 2012], it is therefore necessary to begin the sum at a different index $m_0 > 0$ so that the expression can be successfully calculated. Shnidman [1989] describes a method to determine m_0 given $\tilde{\tau}$ and an acceptable error bound ε. It is also desirable to determine *a priori*, a term m_1 at which the sum will have converged to within ε. This avoids the need to check for convergence at every term added to the sum. These terms can be approximated by a Gaussian for large $\tilde{\tau}$, as shown in Appendix A of [Bocquet 2012]:

$$
e^{-\tilde{\tau}} \frac{\tilde{\tau}^m}{m!} \approx \frac{\exp\left(-\frac{1}{2j}(m - \tilde{\tau})^2 \right)}{\sqrt{2\pi m}}.
\tag{C18}
$$

Hence the error function provides an approximation to the sum:

$$
\sum_{m=0}^{m_1} e^{-\tilde{\tau}} \frac{\tilde{\tau}^m}{m!} \approx \tfrac{1}{2}(1 + \text{erf}(u)) \text{ with } u = (m_1 - \tilde{\tau})/\sqrt{2m_1}.
\tag{C19}
$$

We require

$$
1 - \sum_{m=0}^{m_1} e^{-\tilde{\tau}} \frac{\tilde{\tau}^m}{m!} \approx \tfrac{1}{2}(1 - \text{erf}(u)) < \varepsilon
\tag{C20}
$$

where a lower bound for the error function is given by Nandagopal, Sen & Rawat [2010]:

$$
\sqrt{1 - e^{-u^2}} \leq \text{erf}(u).
\tag{C21}
$$

Thus we can set

$$
\varepsilon = \tfrac{1}{2}\left(1 - \sqrt{1 - e^{-u^2}} \right) \geq \tfrac{1}{2}(1 - \text{erf}(u))
\tag{C22}
$$

and solve for u^2 to get

$$
u^2 = -\ln(4\varepsilon(1 - \varepsilon)) \approx -\ln(4\varepsilon) \equiv G.
\tag{C23}
$$

Finally, m_1 is found from Equations C19 and C23 with the ceiling function applied to get an integer:

$$
m_1 = \left\lceil \tilde{\tau} + G + \sqrt{G(G + 2\tilde{\tau})} \right\rceil.
\tag{C24}
$$

Unfortunately, the approximation in Equation C18 is poor for $m < \tilde{\tau}$, particularly if $\tilde{\tau}$ is small, so the starting term m_0 can be found using a different approximation described by Shnidman [1989]:

$$\sum_{m=0}^{m_0} e^{-\tilde{\tau}} \frac{\tilde{\tau}^m}{m!} \approx \tfrac{1}{2} \left(1 + \mathrm{erf}(u)\right) \ \text{with} \ \sqrt{2}u = \sqrt{\left(m_0 - \tfrac{1}{2}\right)} - \sqrt{2\tilde{\tau} - \left(m_0 - \tfrac{1}{2}\right)}. \tag{C25}$$

Here we require an upper bound for the error function, such as the one given in [Nandagopal, Sen & Rawat 2010]:

$$\sqrt{1 - e^{-4u^2/\pi}} \geq \mathrm{erf}(u) \tag{C26}$$

so we can set

$$\varepsilon = \tfrac{1}{2}\left(1 + \sqrt{1 - e^{-4u^2\pi}}\right) \geq \tfrac{1}{2}\left(1 + \mathrm{erf}(u)\right). \tag{C27}$$

From Equations C25 and C27,

$$u^2 = \frac{\pi}{4}G = G' = \tilde{\tau} - \sqrt{2\tilde{\tau} - \left(m_0 - \tfrac{1}{2}\right)}\sqrt{m_0 - \tfrac{1}{2}}. \tag{C28}$$

Dropping the $1/2$ then gives the solution

$$m_0 = \begin{cases} \left\lfloor \tilde{\tau} - \sqrt{G'(2\tilde{\tau} - G')} \right\rfloor, & \tilde{\tau} > G' \\ 0, & \tilde{\tau} \leq G'. \end{cases} \tag{C29}$$

The parameter ε is set so it is much smaller than the precision of the computer arithmetic (typically $\sim 10^{-16}$ for double precision). For this work, we use $\varepsilon = 10^{-30}$ for which $G \approx 67.7$. Although we have from Equation C28, $G' = \pi G/4 \approx 0.785 G$, we can set $G' = G$ without affecting the accuracy of the result provided ε is much smaller than the computing precision.

DEFENCE SCIENCE AND TECHNOLOGY GROUP DOCUMENT CONTROL DATA	1. DLM/CAVEAT (OF DOCUMENT)

2. TITLE Radar Detection Performance in Medium Grazing Angle X-band Sea-clutter	3. SECURITY CLASSIFICATION (FOR UNCLASSIFIED REPORTS THAT ARE LIMITED RELEASE USE (L) NEXT TO DOCUMENT CLASSIFICATION) Document (U) Title (U) Abstract (U)

4. AUTHORS Luke Rosenberg and Stephen Bocquet	5. CORPORATE AUTHOR Defence Science and Technology Group PO Box 1500 Edinburgh, South Australia 5111, Australia

6a. DST Group NUMBER DST-Group–TR–3193	6b. AR NUMBER 016-484	6c. TYPE OF REPORT Technical Report	7. DOCUMENT DATE December 2015

8. Objective ID AV12605548	9. TASK NUMBER AIR7000	10. TASK SPONSOR DGAD

13. DST Group Publications Repository `http://dspace.dsto.defence.gov.au/dspace/`	14. RELEASE AUTHORITY Chief, National Security and ISR Division

15. SECONDARY RELEASE STATEMENT OF THIS DOCUMENT

Approved for Public Release

OVERSEAS ENQUIRIES OUTSIDE STATED LIMITATIONS SHOULD BE REFERRED THROUGH DOCUMENT EXCHANGE, PO BOX 1500, EDINBURGH, SOUTH AUSTRALIA 5111

16. DELIBERATE ANNOUNCEMENT

No Limitations

17. CITATION IN OTHER DOCUMENTS

No Limitations

18. RESEARCH LIBRARY THESAURUS

Probability distribution, radar, detection, modelling

19. ABSTRACT

This report describes the target detection performance of an airborne surface surveillance radar in the presence of medium grazing angle sea-clutter. In the absence of frequency agility, the temporal correlation of the sea-clutter can be significant and if it is not accounted for in the radar model, the required signal to interference ratio for a given probability of detection, P_d, will be incorrect by several dB, resulting in over-estimated performance. This report describes a robust method for calculating the P_d for both K and Pareto compound sea-clutter distributions. Empirical models of the amplitude distribution and the speckle correlation are used to determine the expected detection performance given different collection geometries and environmental conditions with the output used to determine the minimum detectable target radar cross section in a detection scenario.